




Microphysical Modeling of Mineral Clouds in GJ1214 b and GJ436 b: Predicting Upper Limits on the Cloud-top Height

Kazumasa Ohno and Satoshi Okuzumi 

Department of Earth and Planetary Sciences, Tokyo Institute of Technology, Meguro, Tokyo, 152-8551, Japan

Received 2017 November 22; revised 2018 March 22; accepted 2018 April 15; published 2018 May 21

Abstract

The ubiquity of clouds in the atmospheres of exoplanets, especially of super-Earths, is one of the outstanding issues for the transmission spectra survey. Understanding the formation process of clouds in super-Earths is necessary to interpret the observed spectra correctly. In this study, we investigate the vertical distributions of particle size and mass density of mineral clouds in super-Earths using a microphysical model that takes into account the vertical transport and growth of cloud particles in a self-consistent manner. We demonstrate that the vertical profiles of mineral clouds significantly vary with the concentration of cloud condensation nuclei and atmospheric metallicity. We find that the height of the cloud top increases with increasing metallicity as long as the metallicity is lower than the threshold. If the metallicity is larger than the threshold, the cloud-top height no longer increases appreciably with metallicity because coalescence yields larger particles of higher settling velocities. We apply our cloud model to GJ1214 b and GJ436 b, for which recent transmission observations suggest the presence of high-altitude opaque clouds. For GJ436 b, we show that KCl particles can ascend high enough to explain the observation. For GJ1214 b, by contrast, the height of KCl clouds predicted from our model is too low to explain its flat transmission spectrum. Clouds made of highly porous KCl particles could explain the observations if the atmosphere is highly metal-rich, and hence the particle microstructure might be a key to interpret the flat spectrum of GJ1214 b.

Key words: planets and satellites: atmospheres – planets and satellites: composition – planets and satellites: individual (GJ1214 b, GJ436 b)

1. Introduction

Transmission spectroscopy is one of the powerful approaches to probe the composition of exoplanetary atmospheres (e.g., Seager & Sasselov 2000; Brown 2001). Recent observations of the transmission spectra of super-Earths¹ have revealed that some of them might have hydrogen-rich atmospheres (Fraine et al. 2014; Tsiraras et al. 2016; Southworth et al. 2017; Wakeford et al. 2017). However, it has also been revealed the many super-Earths exhibit featureless spectra that imply the presence of high metallicity atmospheres and/or opaque clouds at high altitude (e.g., Bean et al. 2010; Ehrenreich et al. 2014; Knutson et al. 2014a, 2014b; Kreidberg et al. 2014; Dragomir et al. 2015; Stevenson et al. 2016). Understanding the origin of these high-altitude clouds is important because they might offer important clues on the composition and structure of the atmosphere beneath.

GJ1214 b and GJ436 b are the typical super-Earths that show featureless transmission spectra (e.g., Bean et al. 2010; Berta et al. 2012; Narita et al. 2013; Kreidberg et al. 2014; Knutson et al. 2014a). Kreidberg et al. (2014) measured the near-infrared transmission spectrum of GJ1214 b using the *Hubble Space Telescope* and found that a cloud-free atmosphere cannot explain the featureless spectrum, even if a pure steam atmosphere is assumed. They showed that the presence of an opaque cloud at pressure below 10^{-5} bar is necessary to explain the observed spectrum. Knutson et al. (2014a) measured the transmission spectrum of GJ436 b using the same instrument and found that the planet has a featureless

spectrum that can be explained by high-metallicity ($\sim 1000\times$ solar) atmosphere and/or an opaque cloud at 10^{-3} bar.

One possible mechanism that can form high-altitude clouds in super-Earths is condensation from vapor to particles, followed by upward transport by convection or turbulent diffusion (e.g., Ackerman & Marley 2001), as seen in terrestrial water clouds. In close-in super-Earths where the atmospheric temperature is 500–1000 K, minerals such as KCl and ZnS can condense and form clouds (e.g., Miller-Ricci Kempton et al. 2012). Morley et al. (2013, 2015) investigated the vertical distribution of clouds in GJ1214 b using the cloud model of Ackerman & Marley (2001). They found that mineral clouds can ascend to extremely high altitude, as suggested from the observation of Kreidberg et al. (2014), if a sufficiently low settling velocity for cloud particles is assumed. Since the settling speed generally increases with the size of the particles, the results of Morley et al. (2013, 2015) mean that a high-altitude clouds can form if the cloud particles are sufficiently small. However, because Morley et al. (2013, 2015) parameterized the ratio of the settling velocity to upward velocity as a free parameter, it is still unclear whether the assumed particle size is realistic. Morley et al. (2017) applied the same model to GJ436 b, and found that a very thick cloud is not favored, because such a cloud would obscure the molecular lines seen in the observed emission spectrum (e.g., Stevenson et al. 2010). Charnay et al. (2015a, 2015b) investigated the global cloud distribution in GJ1214 b using a 3D global circulation model (GCM), together with a simple tracer model developed by Parmentier et al. (2013). They showed that the large-scale atmospheric circulation driven by the intense day–night heating contrast can loft cloud particles to altitudes high enough to obscure the spectral feature if the atmospheric metallicity is

¹ In this paper, we refer to super-Earth as a planet larger than Earth but smaller than Neptune in radius. A planet whose size is close to Neptune rather than the Earth is also called a mini-Neptune.

higher than $>100\times$ solar and the particle radius is $\sim 0.5\ \mu\text{m}$. However, the particle size is a free parameter in their studies.

Another candidate for the origin of the flat spectra is organic haze formed through the UV photolysis of carbon-bearing species in the upper atmosphere (Miller-Ricci Kempton et al. 2012). Morley et al. (2013, 2015) suggest that photochemical haze can explain the flat spectrum of GJ1214 b if the haze particles are small and if their production rate is high. Recently, Kawashima & Ikoma (2018) investigated the vertical profiles of haze using both photochemical calculation and particle growth model, and found that the flat transmission spectra would be explained if the haze production rate per unit Ly α intensity is considerably higher than would be expected from Titan’s haze. However, it is yet to be explained why the haze production rate per unit UV irradiation would be so high.

As introduced above, the cloud properties, especially the cloud particle size, for super-Earths are still poorly understood. In this study, we investigate the vertical structure of mineral clouds in GJ1214 b and GJ436 b to understand how the particle size and mass density vary with atmospheric parameters, including the atmospheric metallicity. We apply a 1D cloud model that takes into account the vertical transport, gravitational settling, condensation, and collisional growth of cloud particles in a self-consistent manner. The structure of this paper is as follows. In Section 2, we describe the basic equations and numerical setting. In Section 3, we show the results of calculations and interpretation of the microphysical processes controlling the cloud particle size. In Section 4, we compare the cloud-top height predicted from our model with those inferred from the observations of GJ1214 b and GJ436 b to examine if the flat spectra of these super-Earths are caused by mineral clouds. In Section 5, we mainly discuss how size distribution and particle porosity affect the height of cloud top. Our conclusions are presented in Section 6.

2. Method

2.1. Outline

We extend the microphysical model originally developed by Ohno & Okuzumi (2017) to predict the vertical distributions of a cloud in the atmosphere. The cloud model of Ohno & Okuzumi (2017) adopts a 1D Eulerian framework, and provides the vertical distributions of number (n_c) and mass (ρ_c) densities of cloud particles by taking into account the vertical transport of cloud particles due to the updraft motion and gravitational settling, and the particle growth via condensation and coalescence (see Sections 2.3 and 2.5). In this study, we take into account the vertical transport of cloud particles via eddy diffusion (e.g., Ackerman & Marley 2001).

Following previous studies, such as Charnay et al. (2015a) and Morley et al. (2013, 2015), we consider the clouds composed of solid KCl particles formed through the condensation of KCl vapor. The initial cloud particles are assumed to form at the cloud base through the condensation of vapor onto the small nuclei that already exist in the atmosphere, the process so called heterogeneous nucleation. On Earth, such small nuclei, called the cloud condensation nuclei (CCNs), include sea salt, volcano ash, and dust from the land (Rogers & Yau 1989). The amount of CCNs on exoplanets is still highly uncertain and their composition is also uncertain, and therefore we take the number density of CCNs as a free parameter. The height of the cloud base is determined from the comparison

between the atmospheric temperature and condensation temperature (see Section 2.2). The condensation temperature is defined as the temperature at which the partial pressure of a volatile is equal to its saturation vapor pressure.

Following Ohno & Okuzumi (2017), we assume that the cloud particles have the characteristic radius r_c and corresponding mass $m_c = (4\pi/3)\rho_{\text{int}}r_c^3$, where ρ_{int} is the internal density of the particles. The internal density can vary significantly if the particles grow into porous aggregates (Kataoka et al. 2013). In this study we simply assume $\rho_{\text{int}} = \rho_p$, where ρ_p is the material density of the condensate, but we will discuss the influences of varying the internal density in Section 5.3. Assuming the mass distribution is narrowly peaked at $m \approx m_c$, the number and mass densities are related by $\rho_c = m_cn_c$. Such frameworks are called the double-moment bulk schemes in meteorology (e.g., Ziegler 1985; Ferrier 1994) and the characteristic size method in planetary formation community (e.g., Birnstiel et al. 2012; Ormel 2014; Sato et al. 2016). This method allows us to derive the physical understanding from calculations more clearly, and to perform the calculations with very little computational time compared with spectral bin schemes (e.g., Brauer et al. 2008) that solve the evolution of the full size distribution.

We investigate the influences of atmospheric metallicity on the vertical profiles of clouds in super-Earths. In this paper, the atmospheric metallicity refers to the ratio of atmospheric heavy element abundance to that of the solar atmosphere (i.e., $(N_Z/(N_H + N_{\text{He}}))/(N_Z/(N_H + N_{\text{He}}))_{\text{solar}}$). Recent theoretical studies suggest that the atmospheres of super-Earths potentially have metallicities higher than solar, and even higher than $100\times$ solar, depending on the properties of the building blocks of the respective planets (Fortney et al. 2013; Venturini et al. 2016). Also, the interior modeling showed that GJ1214 b might have a steam atmosphere mainly composed of water vapor (Rogers & Seager 2010; Valencia et al. 2013). Therefore, we take the atmospheric metallicity as a free parameter widely ranging from the metallicity of $1\times$ solar to water vapor atmosphere. The metallicity difference provides the different pressure–temperature structure, total cloud mass, and eddy diffusion coefficient.

2.2. Construction of Vertical Structure

To determine the location of the cloud base, we construct the pressure–temperature structure using the analytical model of radiative atmosphere described by Guillot (2010) under the assumption of hydrostatic equilibrium. Guillot (2010) derived the analytical solution of global mean thermal profiles that gives good agreement with the predictions from sophisticated simulations. The stellar effective temperature, radii, semimajor axis, and planetary radii of GJ1214 b and GJ436 b are taken from the Exoplanet.eu catalog.² Following Guillot (2010), the temperature in each atmospheric layer is given by

$$T^4 = \frac{3T_{\text{int}}^4}{4} \left[\frac{2}{3} + \tau \right] + \frac{3T_{\text{irr}}^4}{4} f \times \left[\frac{2}{3} + \frac{1}{\gamma\sqrt{3}} + \left(\frac{\gamma}{\sqrt{3}} - \frac{1}{\gamma\sqrt{3}} \exp(-\gamma\sqrt{3}\tau) \right) \right], \quad (1)$$

² <http://exoplanet.eu>

where τ is the vertical infrared optical depth τ given by

$$\tau(z) = \int_z^\infty \rho_g \kappa_{\text{th}} dz', \quad (2)$$

where κ_{th} is the atmospheric infrared opacity. The $f = 1/4$ is the heat redistribution factor under the assumption of the radiation redistributed around the entire planet, T_{int} is the intrinsic effective temperature, T_{irr} is the irradiation effective temperature, and the $\gamma = \kappa_v / \kappa_{\text{th}}$ is the ratio of the visible to infrared opacities, respectively. For GJ1214 b, we take $T_{\text{int}} = 60$ K (Rogers & Seager 2010) and $\gamma = 0.038$, so that reproduces the P–T structure predicted by radiative transfer models of Miller-Ricci & Fortney (2010). For GJ436 b, we take $T_{\text{int}} = 300$ K (Morley et al. 2017) and $\gamma = 0.05$ that is in a good agreement with the retrieved P–T structure (Miguel et al. 2015).

We calculate τ using the fitting formula of Rosseland mean opacity of a cloud-free atmosphere described by Freedman et al. (2014). This fitting formula is a function of atmospheric metallicity, pressure, and temperature, and valid for $P = 10^{-6} - 3 \times 10^2$ bar and $T = 75 - 4000$ K. Although the opacity table for higher metallicity ($> 50 \times$ solar) is not available so far, the fitting formula can provide the qualitative results for such high metallicity atmospheres. For water vapor atmospheres, we use the opacity of $50 \times$ solar metallicity that yields the similar P–T structure to that for a water vapor (Miller-Ricci & Fortney 2010) for simplicity. We also neglect the opacity of cloud particles that might change the location of the cloud base, but we plan to investigate these impacts in future study.

Figure 1 shows the vertical P–T structures of GJ1214 b for $1 \times$ and $100 \times$ solar metallicity and the condensation temperature at each atmospheric layer. Here we predict the condensation temperature for each volatile using the saturation vapor pressure described in Rogers & Yau (1989), Ackerman & Marley (2001), and Morley et al. (2012). The vapor species has a solid phase if the atmospheric temperature is lower than its condensation temperature. Therefore, for each volatile species, the cloud base is expected to be placed at the location where the P–T curve intersects the curve of condensation temperature of the species. Figure 1 indicates that the KCl, ZnS, and Na_2S are condensible for $1 \times$ solar metallicity case, and KCl and ZnS are condensible for $100 \times$ solar metallicity. Since the abundance of KCl vapor is higher than that of ZnS vapor for solar like atmosphere (Morley et al. 2012), we focus on the mineral clouds of KCl in this study. The cloud base for KCl is placed at ~ 0.4 bar for $1 \times$ solar metallicity, ~ 0.1 bar for $10 \times$ solar metallicity, and ~ 0.07 bar for $100 \times$ solar metallicity, respectively, which is in good agreement with the prediction of previous studies (Miller-Ricci Kempton et al. 2012; Morley et al. 2013; Charnay et al. 2015a).

2.3. Transport Equations

We calculate the vertical distributions of the number and mass densities of cloud particles by taking into account their growth and vertical transport. The microphysics of cloud formation is complex (see, e.g., Rossow 1978; Rogers & Yau 1989; Pruppacher & Klett 1997; Seinfeld & Pandis 2006). However, Ohno & Okuzumi (2017) showed that inclusion of condensation and collisional growth is enough to approximately reproduce the observations of terrestrial water clouds

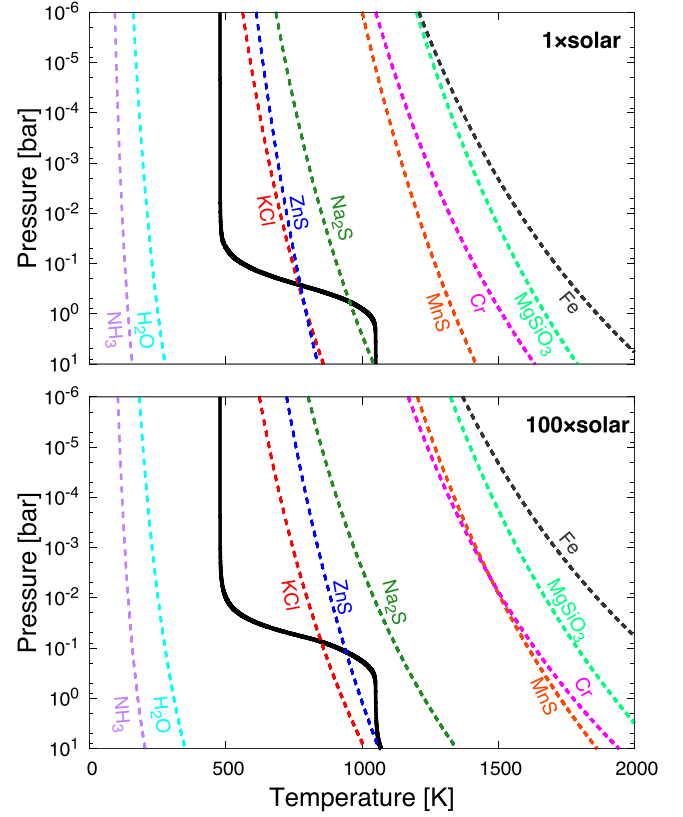


Figure 1. P–T profiles of GJ1214 b and the vapor pressure curves for the metallicity of $1 \times$ solar (top) and $100 \times$ solar (bottom) abundance, respectively. The vapor pressures used in the figures are taken from Rogers & Yau (1989), Ackerman & Marley (2001), and Morley et al. (2012). The solid black lines are the P–T structure, assuming the heat redistribution around the entire planet ($f = 1/4$).

and Jovian ammonia clouds. Therefore we take into account the condensation and collisional growth in this study.

Following Charnay et al. (2015a), we consider the clouds formed through the large-scale atmospheric motion driven by the intense day–night heating contrast. Previous studies showed that the global averaged distributions of such clouds can be approximately reproduced by a 1D advection-diffusion model with an empirical parameterization of the eddy diffusion coefficient K_z (Parmentier et al. 2013; Charnay et al. 2015a). Hence the master equations used here are constructed by adding the source terms expressing particle growth to the 1D advection-diffusion model:

$$\frac{\partial n_c}{\partial t} = \frac{\partial}{\partial z} \left[n_g K_z \frac{\partial}{\partial z} \left(\frac{n_c}{n_g} \right) + v_t(r) n_c \right] - \left| \frac{\partial n_c}{\partial t} \right|_{\text{coll}}, \quad (3)$$

$$\frac{\partial \rho_c}{\partial t} = \frac{\partial}{\partial z} \left[\rho_g K_z \frac{\partial}{\partial z} \left(\frac{\rho_c}{\rho_g} \right) + v_t(r) \rho_c \right] + \left(\frac{\partial \rho_c}{\partial t} \right)_{\text{cond}}, \quad (4)$$

$$\frac{\partial \rho_v}{\partial t} = \frac{\partial}{\partial z} \left[\rho_g K_z \frac{\partial}{\partial z} \left(\frac{\rho_v}{\rho_g} \right) \right] - \left(\frac{\partial \rho_v}{\partial t} \right)_{\text{cond}}, \quad (5)$$

where v_t is the terminal velocity of cloud particles, K_z is the eddy diffusion coefficient, and ρ_v is the vapor mass density. The terminal velocity depends on the particle size and atmospheric density, as introduced in Section 2.4. Each source term, introduced in Section 2.5, expresses the particle growth

Table 1
Model Parameters for GJ1214 b

Metallicity	H (km)	q_{KCl} (mol/mol)	K_0 ($\text{m}^2 \text{s}^{-1}$)	Δz (km)
$1 \times \text{solar}$	190	2.54×10^{-7}	7.0×10^2	20
$10 \times \text{solar}$	180	2.52×10^{-6}	2.8×10^3	20
$100 \times \text{solar}$	103	2.32×10^{-5}	3.0×10^3	10
Steam	25	2.61×10^{-4}	3.0×10^2	5

via condensation and collision of each particle. Without these terms, the Equations (3)–(4) are reduced to the 1D transport model for fixed size particles used by Parmentier et al. (2013) and Charnay et al. (2015a).

The eddy diffusion coefficient K_z represents the strength of effective vertical mixing for cloud particles. In this study, we adopt the empirical formula of K_z proposed by Charnay et al. (2015a),

$$K_z = K_0 \left(\frac{P}{P_0} \right)^{-2/5}, \quad (6)$$

where K_0 is the value of K_z at a reference pressure P_0 . Charnay et al. (2015a) derived this formula from 3D GCM simulations that takes into account the transport of fixed size particles. Since they suggested that K_z is almost independent of particle size (see the Figure 14 of Charnay et al. 2015a), we use Equation (6) for all ranges of particle size in our calculations. The exponent of $-2/5$ is similar to the $K_z \propto P^{-1/3}$ predicted by mixing theory (Ackerman & Marley 2001) and $K_z \propto P^{-1/2}$ predicted by other GCM simulations for hot Jupiter (Parmentier et al. 2013). According to Charnay et al. (2015a), we choose the reference pressure of $P_0 = 1$ bar and take the values of K_0 as summarized in Tables 1 and 2. For GJ1214 b, we use the values of K_0 derived from the power-law fitting to the GCM data (see Figure 14 of Charnay et al. 2015a), which are metallicity-dependent. For GJ436 b, we adopt $K_0 = 2.5 \times 10^3 \text{ m}^2 \text{s}^{-1}$ independent of the metallicity. The adopted value is similar to the value $K_z \sim 10^2\text{--}10^3 \text{ m}^2 \text{s}^{-1}$ suggested by Madhusudhan & Seager (2011) to explain the disequilibrium chemistry seen in GJ436 b's emission spectra. Our adopted value is two orders of magnitude lower than the earlier prediction by Lewis et al. (2010) based on the rms velocity from 3D GCM calculations. However, Parmentier et al. (2013) and Charnay et al. (2015a) recently pointed out that the values of the eddy diffusion coefficient predicted in this way tend to be one or two orders of magnitude higher than those directly determined from vertical particle distribution. If we take this into account, our choice of K_0 is consistent with the GCM results by Lewis et al. (2010).

2.4. Expression of the Terminal Velocity

A terminal velocity v_t is determined by the balance between gravitational force and gas frictional force. The gas frictional force depends on the behavior of the gas flow around the settling particles, and varies with the particle size, settling velocity, and the mean free path of gas particles (e.g., Rossow 1978; Woitke & Helling 2003). In this study, we

Table 2
Model Parameters for GJ436 b

Metallicity	H (km)	q_{KCl} (mol/mol)	K_0 ($\text{m}^2 \text{s}^{-1}$)	Δz (km)
$1 \times \text{solar}$	169	2.54×10^{-7}	2.5×10^3	20
$10 \times \text{solar}$	159	2.52×10^{-6}	2.5×10^3	20
$100 \times \text{solar}$	102	2.32×10^{-5}	2.5×10^3	10
$1000 \times \text{solar}$	22	2.61×10^{-4}	2.5×10^3	5

adopt the following formula of the terminal velocity,

$$v_t(r_c) = \frac{2\beta g r_c^2 \rho_p}{9\eta} \left[1 + \left(\frac{0.45 g r_c^3 \rho_g \rho_p}{54\eta^2} \right)^{2/5} \right]^{-5/4}, \quad (7)$$

where η is the dynamic viscosity of the atmosphere and β is the *slip correction factor*. β accounts for the transition of gas drag behavior from viscous flow (Stokes's law) to free molecular flow (Epstein's law) around the particle, given by (Davies 1945)

$$\beta = 1 + \text{Kn}_g [1.257 + 0.4 \exp(-1.1/\text{Kn}_g)], \quad (8)$$

where $\text{Kn}_g = l/r_c$ is the gas Knudsen number and l is the gas mean free path given in the Appendix. Equation (7) without β is same as the Equation (23) in Ohno & Okuzumi (2017) that asymptotically reaches the Stokes's law for a laminar flow limit, Newton's law for a turbulent flow limit, and reproduces the intermediate regime predicted by the experiment (see the Figure 7 in Ohno & Okuzumi 2017). The top panel of Figure 2 shows the terminal velocity as a function of particle size and atmospheric pressure. Figure 2 shows the terminal velocity increases with height in the upper atmosphere because of Epstein's law arisen from the low atmospheric density.

We also show the ratio of the mixing timescale τ_{mix} to the falling timescale τ_{fall} in the bottom panel of Figure 2. Each timescale is defined as

$$\tau_{\text{mix}} = \frac{H^2}{K_z} \quad (9)$$

and

$$\tau_{\text{fall}} = \frac{H}{v_t}, \quad (10)$$

where $H = k_B T / m_g g$ is the pressure scale height, respectively. Here we assume $T = 500$ K, $K_0 = 10^3 \text{ m}^2 \text{s}^{-1}$, and a solar composition atmosphere. Cloud particles ascend if $\tau_{\text{mix}} \ll \tau_{\text{fall}}$, and fall if $\tau_{\text{mix}} \gg \tau_{\text{fall}}$. Figure 2 indicates that the cloud particles are required to maintain their size $r_c \lesssim 5 \mu\text{m}$ to ascend above 10^{-3} bar suggested for GJ436 b (Knutson et al. 2014a), and $r \lesssim 0.3 \mu\text{m}$ to ascend above 10^{-5} bar under the assumed parameters.

2.5. Microphysics of Particle Growth

The cloud particles ascend from the cloud base while growing through condensation and collision with each other. Condensation dominates the growth of small particles due to the relatively short timescale. The growth rate of ρ_c via condensation depends on the behavior of vapor molecule motion, and is expressed by (Rogers & Yau 1989; Woitke &

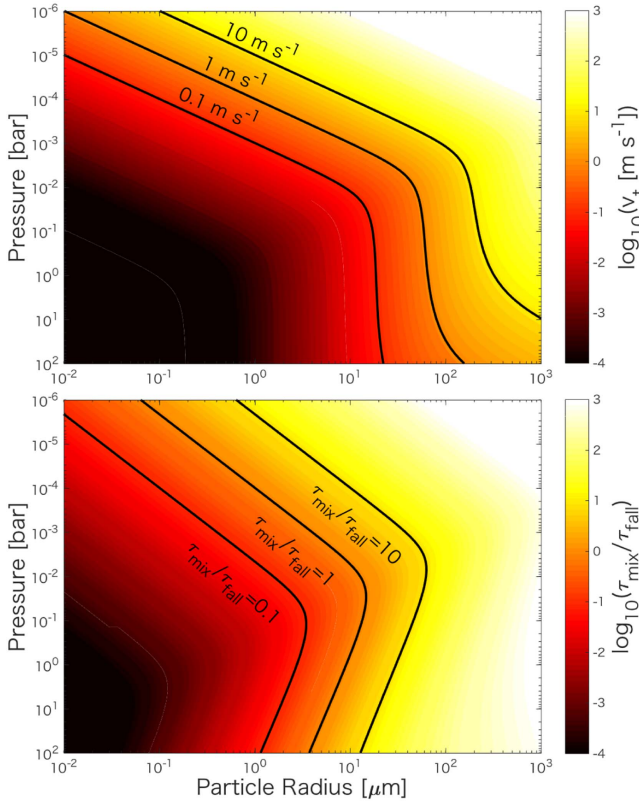


Figure 2. Terminal velocity of compact KCl particles (colorscale, top panel) and the ratio of the mixing timescale to the falling timescale (colorscale, bottom panel). The horizontal axis shows particle radius, and the vertical axis shows atmospheric pressure, respectively. Each black contour shows the pressure and particle radius corresponding to $v_t = 0.1, 1$, and 10 m s^{-1} for the top panel, and $\tau_{\text{mix}}/\tau_{\text{fall}} = 0.1, 1$, and 10 for the bottom panel, respectively. Here we assume $1 \times$ solar metallicity, $K_0 = 10^3 \text{ m}^2 \text{ s}^{-1}$, and isothermal ($T = 500 \text{ K}$) atmosphere.

Helling 2003)

$$\left(\frac{\partial \rho_c}{\partial t}\right)_{\text{cond}} = 4\pi r_c^2 n_c (\rho_v - \rho_s) \times \min \left[C_{\text{re}}, \frac{D}{r_c} \left(1 + \left(\frac{m_v L}{k_B T} - 1 \right) \frac{LD\rho_s}{KT} \right)^{-1} \right], \quad (11)$$

where ρ_v is the vapor mass density, ρ_s is the saturation vapor density, $C_{\text{re}} = \sqrt{k_B T / 2\pi m_v}$ is the relative velocity of vapor molecules, m_v is the mass of the vapor molecules, L is the specific latent heat of condensation, and D is the molecular diffusion coefficient of vapor in ambient air, respectively. The first formula in the bracket corresponds to the free molecular flow regime (Woitke & Helling 2003) in which the vapor molecules are freely impinging onto the particles. The second formula corresponds to the diffusive regime (Rogers & Yau 1989) in which the vapor molecules behave as continuum.

Collisional growth is induced by the relative velocity arisen from both gravitational settling and Brownian motion of particles. In this paper, we refer to the collisional growth by gravitational settling as *coalescence* and that by Brownian motion as *coagulation*. Then the decrease in number density

via collisional growth is expressed by

$$\left| \frac{\partial n_c}{\partial t} \right|_{\text{coll}} = \left| \frac{\partial n_c}{\partial t} \right|_{\text{coag}} + \left| \frac{\partial n_c}{\partial t} \right|_{\text{coal}}, \quad (12)$$

where $|\partial n_c / \partial t|_{\text{coag}}$ is the decrease in number density for coagulation and $|\partial n_c / \partial t|_{\text{coal}}$ is that for coalescence. The expression of $|\partial n_c / \partial t|_{\text{coag}}$ depends on the particle Knudsen number Kn_p defined as

$$\text{Kn}_p = \frac{\beta}{6\eta r_c^2} \sqrt{\frac{m_c k_B T}{2\pi}}. \quad (13)$$

The Brownian motion of particles is diffusive for $\text{Kn}_p \ll 1$ and ballistic for $\text{Kn}_p \gg 1$. The rate of decrease of particle number density via coagulation is given by (Seinfeld & Pandis 2006)

$$\left| \frac{\partial n_c}{\partial t} \right|_{\text{coag}} = \begin{cases} 8 \sqrt{\frac{\pi k_B T}{m_c}} r_c^2 n_c^2 & (\text{Kn}_p > 1/\sqrt{2}) \\ \frac{4k_B T \beta}{3\eta} n_c^2 & (\text{Kn}_p < 1/\sqrt{2}). \end{cases} \quad (14)$$

The transition takes place at $r_c \approx 0.07 \mu\text{m}$ under the assumptions of $T = 1000 \text{ K}$, $P = 0.1 \text{ bar}$, and $m_g = 2 \text{ amu}$, which are equivalent to the parameters for the cloud base.

For the coalescence growth, the rate of decrease of number density $|\partial n_c / \partial t|_{\text{coal}}$ is given by (Rossow 1978)

$$\left| \frac{\partial n_c}{\partial t} \right|_{\text{coal}} \approx 2\pi r_c^2 n_c^2 \Delta v E, \quad (15)$$

where Δv is the relative velocity induced by the gravitational settling, and E is the collection efficiency defined as the ratio of the effective collisional cross section to the geometric cross section (e.g., Pruppacher & Klett 1997). For the relative velocity, Sato et al. (2016) and Krijt et al. (2016) showed that the characteristic size approach with $\Delta v = 0.5v_t(r)$ is in good agreement with the results of spectral bin schemes, and therefore we assume $\Delta v = 0.5v_t(r_c)$. The collection efficiency E accounts for the effect of the gas flow around the particle moving relative to the background gas, and is expressed in terms of Stokes number

$$\text{Stk} = \frac{v_t(r_c) \Delta v}{g r_c}, \quad (16)$$

which is defined as the ratio of the stopping time $= v_t(r_c)/g$ to the crossing time $\sim r_c/\Delta v$. When $\text{Stk} \ll 1$, the particles are strongly coupled to the gas flow around the other particles, and hence E behaves as $E \approx 0$ (Rossow 1978). We evaluate E using a smoother analytic function of Guillot et al. (2014) given by

$$E = \max[0, 1 - 0.42\text{Stk}^{-0.75}], \quad (17)$$

which vanishes at $\text{Stk} \lesssim 0.3$ and approaches unity at $\text{Stk} \gg 1$. If $\text{Kn}_g > 1$, we assume $E = 1$ because the influence of the gas on the particle trajectory should be weak in that region (Rossow 1978).

2.6. Numerical Procedure

We numerically solve the Equations (3)–(5) until the system reaches to the steady-state profiles. The initial number density

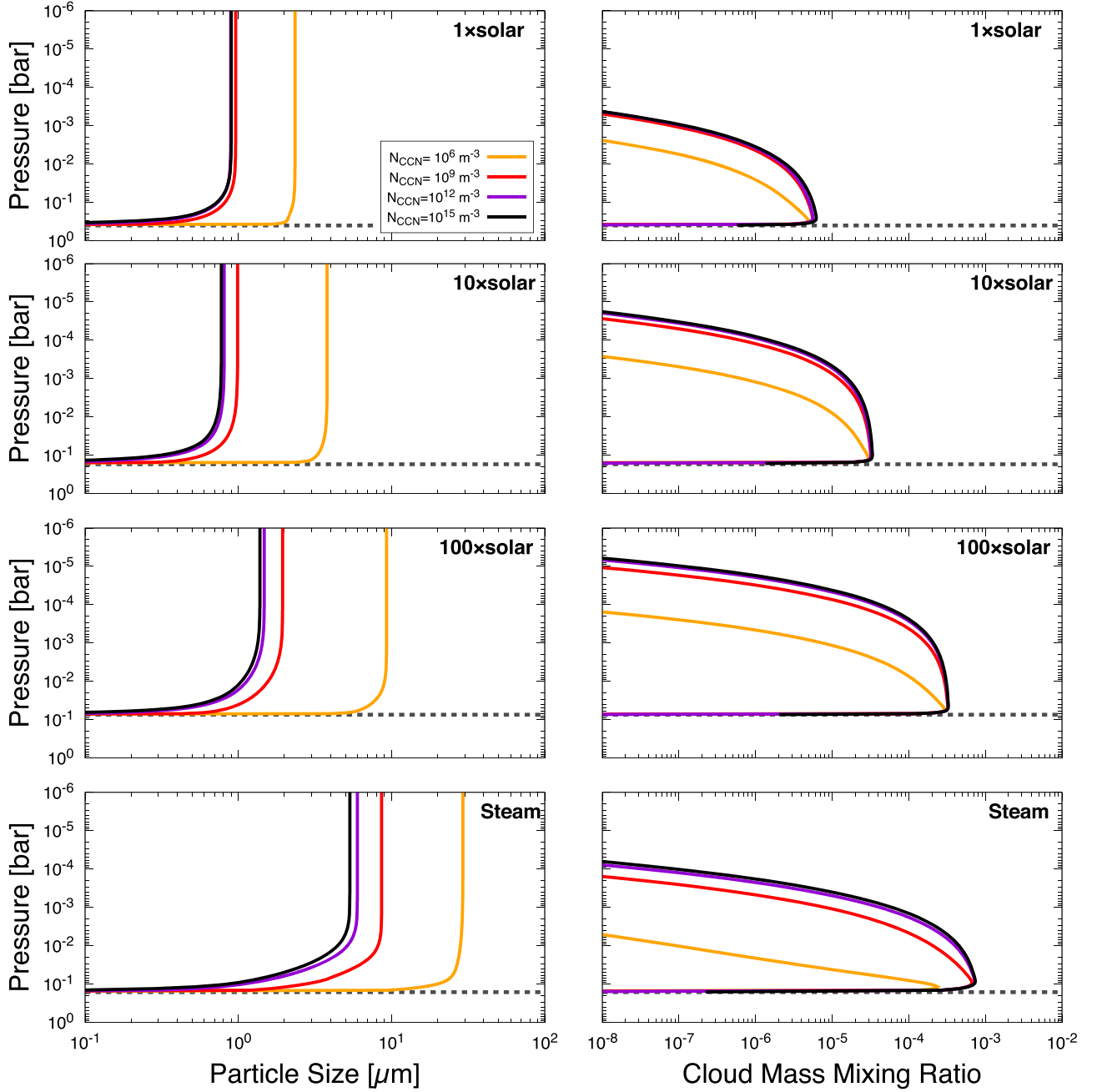


Figure 3. Vertical structure of the KCl cloud for different atmospheric metallicity models. The left and right columns show the vertical distributions of the particle radius and mass mixing ratio, respectively, for different values of the CCN number density n_{CCN} . Each row, from top to bottom, is for atmospheric metallicities of 1 \times , 10 \times , 100 \times solar, and steam atmosphere, respectively. The orange, red, purple, and black lines show the results for $n_{\text{CCN}} = 10^6, 10^9, 10^{12},$ and 10^{15} m^{-3} , respectively. The gray dotted lines indicate the cloud base.

of the cloud particles at the cloud base is parameterized by the CCN number density n_{CCN} . We take the n_{CCN} as a free parameter widely ranging as 10^6 – 10^{15} m^{-3} . Since the composition of the CCNs in close-in super-Earths is unknown, we assume the bulk density of the CCNs as that of KCl. This assumption does not affect the calculated cloud vertical profiles as long as the mass fraction of the CCNs in the cloud particles is very small. Therefore, we choose the upper limit of n_{CCN} so that the total mass of CCNs does not exceed that of KCl vapor at the cloud base. We set the radii of CCNs as $r_{\text{CCN}} = 0.001 \mu\text{m}$, and then $n_{\text{CCN}} \approx 10^{15} \text{ m}^{-3}$ corresponds to the upper limit for our calculations.

We choose the flux of a lower boundary condition so that n_c/n_g , ρ_c/ρ_g , and ρ_v/ρ_g keep the values of the cloud base. We adopt the zero-flux boundary condition at the top of the computational domain, which is located at $P = 10^{-8}$ bar. The vertical coordinate z is discretized into linearly spaced bins. We use the different grid width for different atmospheric metallicity, as summarized in Table 1. The time increment Δt is chosen at every time step so that the fractional decreases in n , ρ_c , and ρ_v do not exceed 0.5 (i.e., $\Delta t \leq -0.5 \times \min[(\partial \ln n / \partial t)^{-1}, (\partial \ln \rho_c / \partial t)^{-1}, (\partial \ln \rho_v / \partial t)^{-1}]$). However, this expression yields very small Δt because the time increment determined by condensation is much shorter than that for

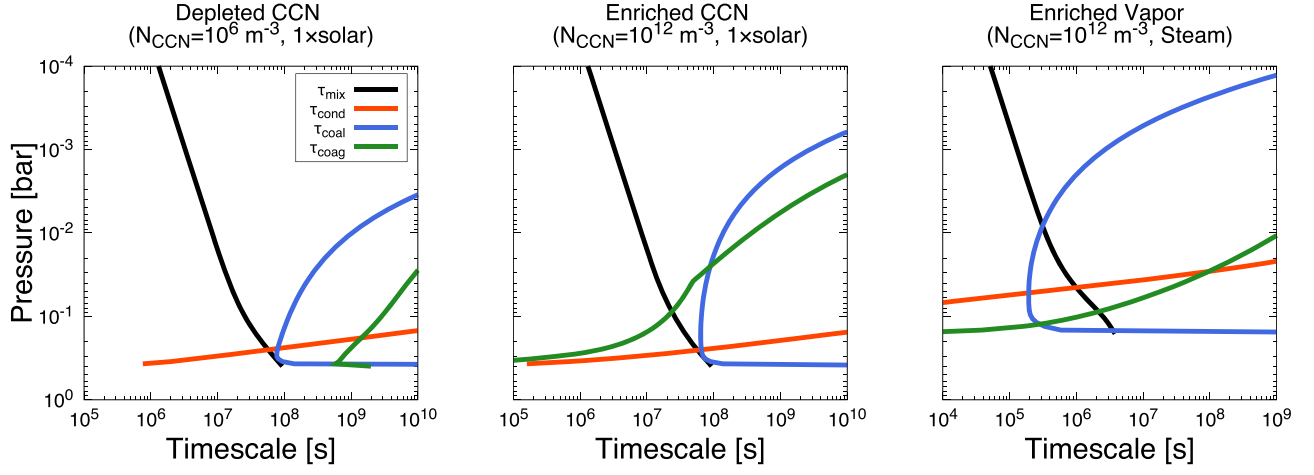


Figure 4. Vertical distributions of the timescales of particle growth and vertical mixing. The left, middle, and right panels show the distributions for $n_{\text{CCN}} = 10^6$ and 10^{12} m^{-3} with the metallicities of $1 \times$ solar, and $n_{\text{CCN}} = 10^{12} \text{ m}^{-3}$ with the pure steam atmosphere. The black, red, blue, and green lines show the timescales of vertical mixing, condensation, coalescence, and coagulation, respectively.

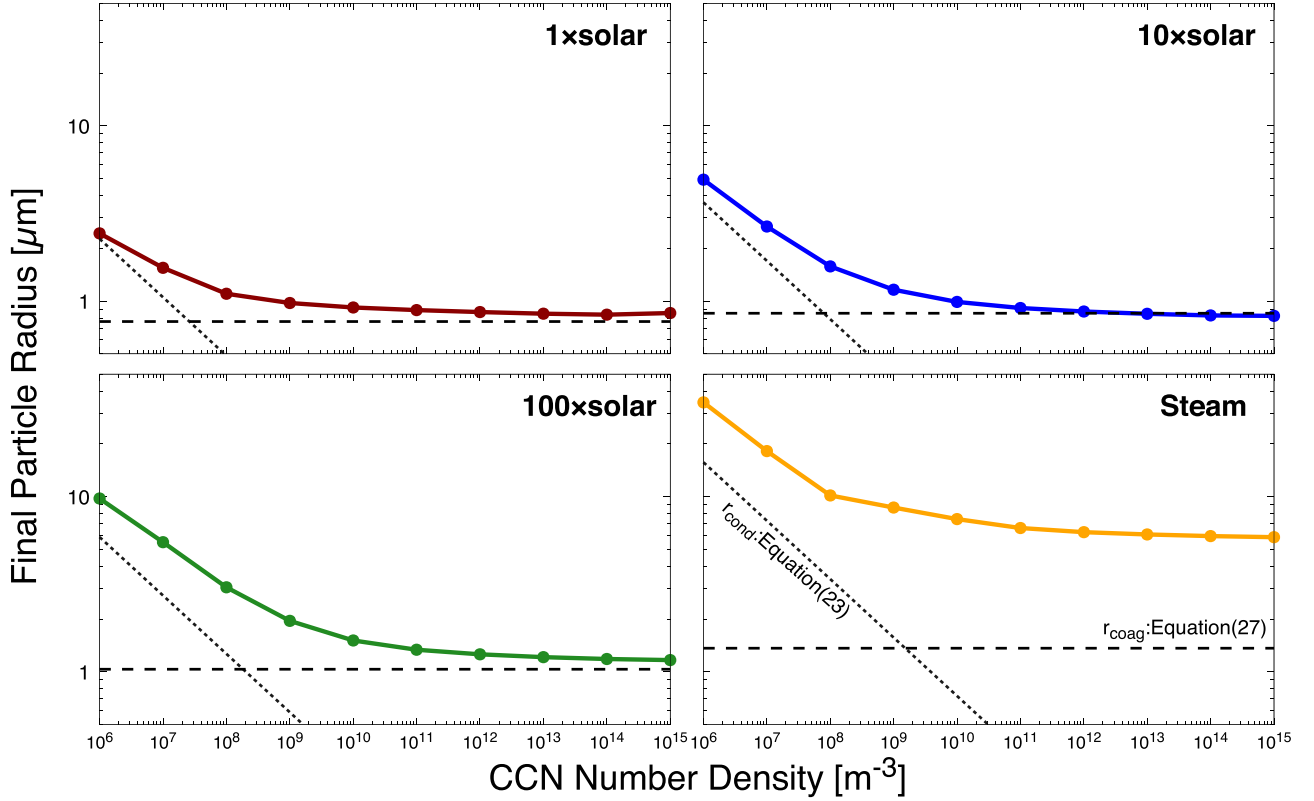


Figure 5. Final particle radius as a function of the CCN number density. From top to bottom, each row shows the final radius for the metallicity of $1 \times$, $10 \times$, $100 \times$ solar, and the steam atmosphere, respectively. The dashed and dotted lines show the size determined by coagulation, r_{coag} , predicted by Equation (27) and that by condensation, r_{cond} , predicted by Equation (23), respectively (see Sections 3.2.1 and 3.2.2).

collisional growth and vertical transport. To avoid this, we adjust the time increment as $\Delta t \leq -0.5 \times (\partial \ln n / \partial t)^{-1}$ if $(\partial \ln \rho_c / \partial t)^{-1} < 0.1 \times (\partial \ln n / \partial t)^{-1}$. In this case, we convert the all excess/lack of vapor from saturation value into cloud particles.

We calculate the mean molecular weight of the atmosphere assuming a hydrogen–helium–water mixture in accordance with Fortney et al. (2013). Elemental abundances are taken from Lodders (2003). The mixing ratio of KCl vapor q_{KCl} below the

cloud base is calculated assuming the number of KCl molecules is equal to that of K. For the steam atmosphere and the metallicity of $1000 \times$ solar, we evaluate the mean molecular weight as that of water, and q_{KCl} as a ratio of K to O because the atmosphere is dominated by water rather than hydrogen for extremely metal-enriched cases. The Appendix summarizes the evaluation of other physical parameters (e.g., viscosity) required for our calculations. Tables 1 and 2 show the values of q_{KCl} , K_0 , and H at the upper isothermal region for GJ1214 b and GJ436 b, respectively.

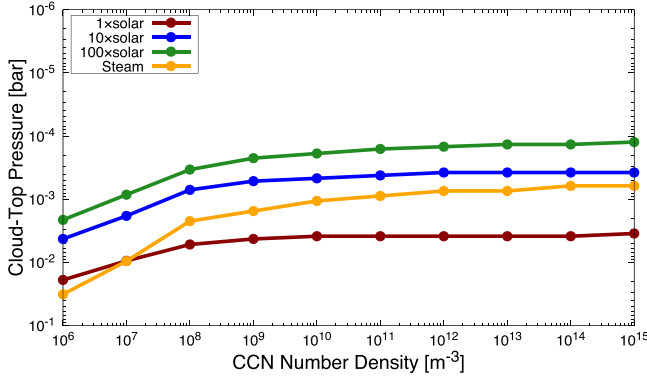


Figure 6. Cloud-top pressure as a function of CCN number density for different atmosphere models. The red, blue, green, and yellow lines are for 1×, 10×, 100× solar models, and pure steam atmosphere, respectively.

3. Results

3.1. Vertical Distribution of the Particle Size and Mass Density

In this section, we particularly focus on the physical mechanisms that control the vertical distributions of the cloud particle size. Figure 3 shows the calculated vertical profiles of mineral clouds in GJ1214 b. We find that the particles grow mainly near the cloud base (left column in Figure 3) and stop growing in the upper atmosphere where $P \leq 10^{-3}$ bar. This occurs because the mixing timescale $\tau_{\text{mix}} \propto K_z^{-1} \propto P^{2/5}$ decreases with height, and eventually becomes shorter than the timescales of condensation, coagulation, and coalescence. This trend is also seen in the results of a recent cloud model that takes into account the evolution of particle size distribution (Gao et al. 2018). The final particle radius ranges from 1 to 2 μm for the metallicity of 1× solar, 0.9–4 μm for 10× solar, 1.5–10 μm for 100× solar, and 5–30 μm for water vapor atmosphere, respectively. Figure 3 indicates that the final particle size decreases with the n_{CCN} and approaches a minimum value in the limit of high n_{CCN} . In Section 3.2 we explain how the final particle size is determined. We also find that a higher metallicity leads to a larger final size, although its effect is small compared with that of CCN number density.

The cloud mass mixing ratio, defined as ρ_c/ρ_g , steeply decreases with height above the height where $\tau_{\text{fall}} < \tau_{\text{mix}}$. This can be understood from the transport equations. In the upper atmosphere, the source terms expressing the particle growth are negligible, as mentioned above. Therefore, in a steady state, the vertical mixing of particles should balance with sedimentation,

$$-\rho_g K_z \frac{\partial}{\partial z} \left(\frac{\rho_c}{\rho_g} \right) - v_t \rho_c = 0. \quad (18)$$

When the $\tau_{\text{mix}} \ll \tau_{\text{fall}}$, Equation (18) indicates that ρ_c/ρ_g is nearly constant for height, which is seen in the lower region of Figure 3. When the $\tau_{\text{mix}} \gg \tau_{\text{fall}}$, the mass mixing ratio decreases with height due to the particle sedimentation.

The vertical distribution of the cloud mass density also depends on the CCN number density and atmospheric metallicity (the right column of Figure 3). A larger CCN number density leads to a higher mass density at high altitude, because the final particle size decreases with n_{CCN} as mentioned before. We also find that a higher metallicity yields a higher cloud mass density at high altitude. This metallicity dependence arises because the final particle size is

insensitive to the metallicity, while the cloud mass density at the cloud base is approximately proportional to the metallicity. Furthermore, the dependence of $\tau_{\text{mix}} \propto H^2$ also yields the higher cloud mass at high altitude for higher metallicity cases, because the H decreases with increasing atmospheric metallicity.

3.2. The Mechanisms Controlling Particle Size

The final particle size determines how high the cloud particles can ascend. Here we discuss the mechanisms that control the final particle size. Figure 4 shows the vertical distributions of the timescales of vertical mixing, condensation, coagulation, and coalescence for three cases: depleted CCNs ($n_{\text{CCN}} = 10^6 \text{ m}^{-3}$), enriched CCNs ($n_{\text{CCN}} = 10^{12} \text{ m}^{-3}$), and enriched vapor (steam atmospheres). The timescales of condensation, coagulation, and coalescence are defined as

$$\tau_{\text{cond}} = \rho_c \left| \frac{\partial \rho_c}{\partial t} \right|_{\text{cond}}^{-1}, \quad (19)$$

$$\tau_{\text{coag}} = n_c \left| \frac{\partial n_c}{\partial t} \right|_{\text{coag}}^{-1}, \quad (20)$$

$$\tau_{\text{coal}} = n_c \left| \frac{\partial n_c}{\partial t} \right|_{\text{coal}}^{-1}, \quad (21)$$

and the mixing timescale τ_{mix} is given by Equation (9). Generally, cloud particles grow if $\min(\tau_{\text{cond}}, \tau_{\text{coag}}, \tau_{\text{coal}}) \ll \tau_{\text{mix}}$, and ascend without significant growth if $\min(\tau_{\text{cond}}, \tau_{\text{coag}}, \tau_{\text{coal}}) \gg \tau_{\text{mix}}$. The mixing timescale τ_{mix} decreases with height as mentioned before, whereas the growth timescales increase with height because they are inversely proportional to the density. Hence the particle growth becomes relatively less effective as the particles ascend. In following subsections, we characterize the particle growth in three cases based on timescale argument.

3.2.1. Depleted CCN Regime ($\tau_{\text{mix}} < \tau_{\text{coag}}, \tau_{\text{coal}}$)

In the example shown in the left panel of Figure 4, τ_{cond} is much shorter than τ_{mix} and other growth timescales at the cloud base. The short τ_{cond} results in the quick growth of particles near the cloud base, as shown in Figure 3. At the same time, the rapid condensation also results in rapid depletion of condensing vapor. This depletion eventually suppresses the condensation growth, and hence the total cloud mass at the cloud base is limited by the total amount of condensing vapor there (i.e., $\rho_c(z_b) \approx \rho_v(z_b) = \rho_s(z_b)$).

If n_{CCN} is so small that $\min(\tau_{\text{coal}}, \tau_{\text{coag}}) > \tau_{\text{mix}}$ at the cloud base, the particles start to ascend as soon as the condensation growth is completed (the left column in Figure 4). In this case, the final particle size r_{cond} is determined by the deposition of available vapor onto CCNs—that is,

$$\frac{4}{3} \pi r_{\text{cond}}^3 \rho_p n_{\text{CCN}} \approx \rho_s(z_b), \quad (22)$$

and thus

$$r_{\text{cond}} \approx \left[\frac{3 \rho_s(z_b)}{4 \pi \rho_p n_{\text{CCN}}} \right]^{1/3}, \quad (23)$$

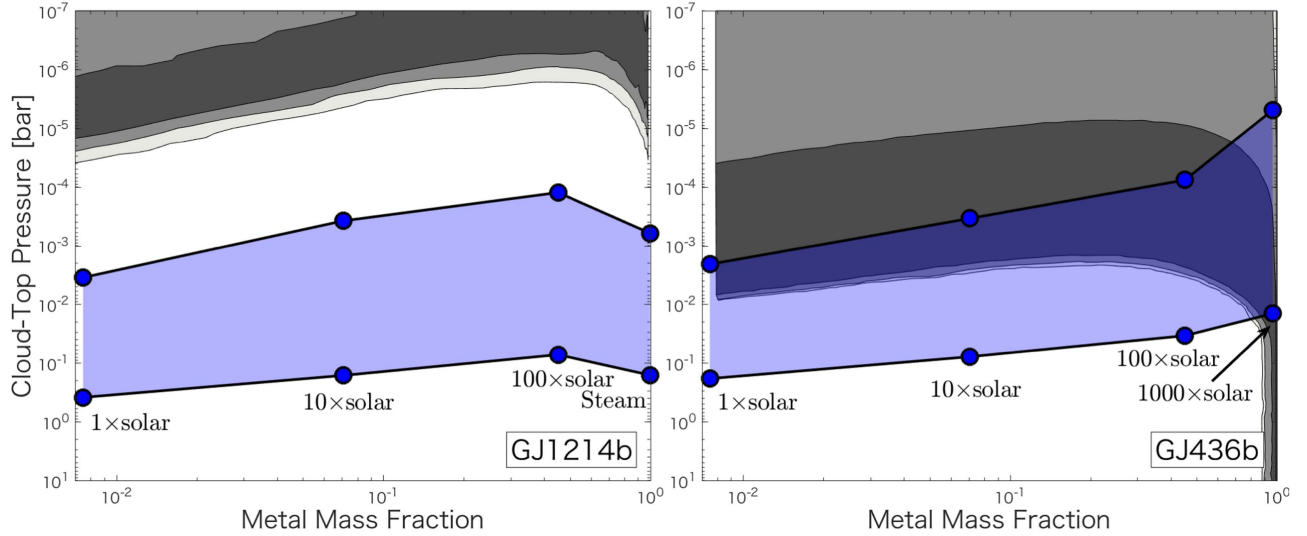


Figure 7. Predicted maximum extent of the KCl cloud for GJ1214 b (left panel) and GJ436 b (right panel) as a function of the metal mass fraction. The dots correspond to, from left to right, hydrogen-rich atmosphere at 1×, 10×, 100× solar metallicity, and pure steam atmosphere for GJ1214 b and 1000× solar metallicity for GJ436 b, respectively. The lower line indicates the height (in pressure) of the cloud base, while the upper line indicates the maximum height of the cloud top for fixed metallicity. The gray-shaded area indicates the location of the cloud top inferred from the Bayesian analysis of the transmission spectrum by Kreidberg et al. (2014) for GJ1214 b and by Knutson et al. (2014a) for GJ436 b, with the black contours marking the 1σ, 2σ, and 3σ Bayesian credible regions.

where we have assumed the initial CCN mass density is much smaller than $\rho_s(z_b)$. Figure 5 shows the final particle size and r_{cond} for each metallicity case. As shown in Figure 5, the final particle size approaches r_{cond} for lower CCN number density. Hence Equation (23) explains why the final particle size decreases with the increasing of CCN number density. Equation (23) also explains the results of Gao et al. (2018), who found that the efficient homogeneous nucleation (high particle number density) results in small particle size.

3.2.2. Enriched CCN Regime ($\tau_{\text{coag}} < \tau_{\text{mix}} < \tau_{\text{coal}}$)

Coagulation leads the further growth of cloud particles in addition to condensation if n_{CCN} is so high that $\tau_{\text{coag}} < \tau_{\text{mix}}$ at the cloud base (see the middle panel of Figure 4). When coagulation is effective, the final particle size becomes larger than r_{cond} and eventually reaches the minimum value in the limit of high CCN number density, as seen in Figure 3. Hence we can expect the particle size must be larger than the minimum value determined by coagulation, even if the CCN number density is uncertain.

The minimum particle size can be analytically estimated in the following way. Because the final particle size ranges as $r > 0.07 \mu\text{m}$ in Figure 3, the coagulation growth falls into diffusive regime, and the τ_{coag} is written by

$$\tau_{\text{coag}} = \frac{3\eta}{4k_B T \beta n_c}. \quad (24)$$

Also, the slip factor can be approximated as $\beta \approx \beta_\infty \text{Kn}_g$, where $\beta_\infty = 1.657$, because the mean free path near the cloud base ($l \sim 10 \mu\text{m}$) is larger than the particle radius (i.e., $\text{Kn}_g \gg 1$). Using the relation $4\pi r_c^3 \rho_p n_c / 3 = \rho_c$ and $\eta = \rho_g v_{\text{th}} l / 3$ (Woitke & Helling 2003), where $v_{\text{th}} = \sqrt{8k_B T / \pi m_g}$ is the mean thermal velocity, the coagulation

timescale can be rewritten as

$$\begin{aligned} \tau_{\text{coag}} &= \frac{\rho_g v_{\text{th}} r_c}{4k_B T \beta_\infty n_c} \\ &= \frac{\pi \rho_p v_{\text{th}}}{3k_B T \beta_\infty q_c} r_c^4, \end{aligned} \quad (25)$$

where $q_c \equiv \rho_c / \rho_g$ is the cloud mass mixing ratio. Because ρ_c is determined by saturation vapor density at the cloud base (see Section 3.2.1), $q_c = \rho_s(z_b) / \rho_g(z_b) = m_{\text{KCl}} q_{\text{KCl}} / m_g$, where m_{KCl} is the mass of a KCl molecule. Coagulation growth completes when the vertical mixing becomes more efficient, and hence the final size is determined from the condition $\tau_{\text{coag}} = \tau_{\text{mix}}$. Equating Equations (25) and (9), the final particle size determined by coagulation r_{coag} is predicted as

$$r_{\text{coag}} = \left(\frac{3\beta_\infty}{\sqrt{8\pi}} \frac{m_{\text{KCl}} q_{\text{KCl}}}{\rho_p K_z(z_b)} g^{1/2} H^{5/2} \right)^{1/4} \left(\frac{P_*}{P_b} \right)^{1/10}, \quad (26)$$

where P_b is the pressure of the cloud base and P_* is the pressure in which the coagulation growth is completed. Equation (26) implies the final particle size in this regime is almost independent of n_{CCN} , because P_* is insensitive to the choice of n_{CCN} , as seen in Figure 4. This explains why the final particle size is almost independent of n_{CCN} for high CCN number density in Figure 3. Particularly, we find that Equation (26) is in good agreement with the minimum final size derived from the numerical results if we assume $P_* = 0.1P_b$. In this case, Equation (26) can be rewritten as the following useful formula

$$\begin{aligned} r_{\text{coag}} &= 1.25 \mu\text{m} \\ &\times \left(\frac{g}{10 \text{ m s}^{-2}} \right)^{1/8} \left(\frac{H}{10^2 \text{ km}} \right)^{5/8} \\ &\times \left(\frac{K_z(z_b)}{10^3 \text{ m}^2 \text{ s}^{-1}} \right)^{-1/4} \left(\frac{q_{\text{KCl}}}{10^{-5}} \right)^{1/4}. \end{aligned} \quad (27)$$

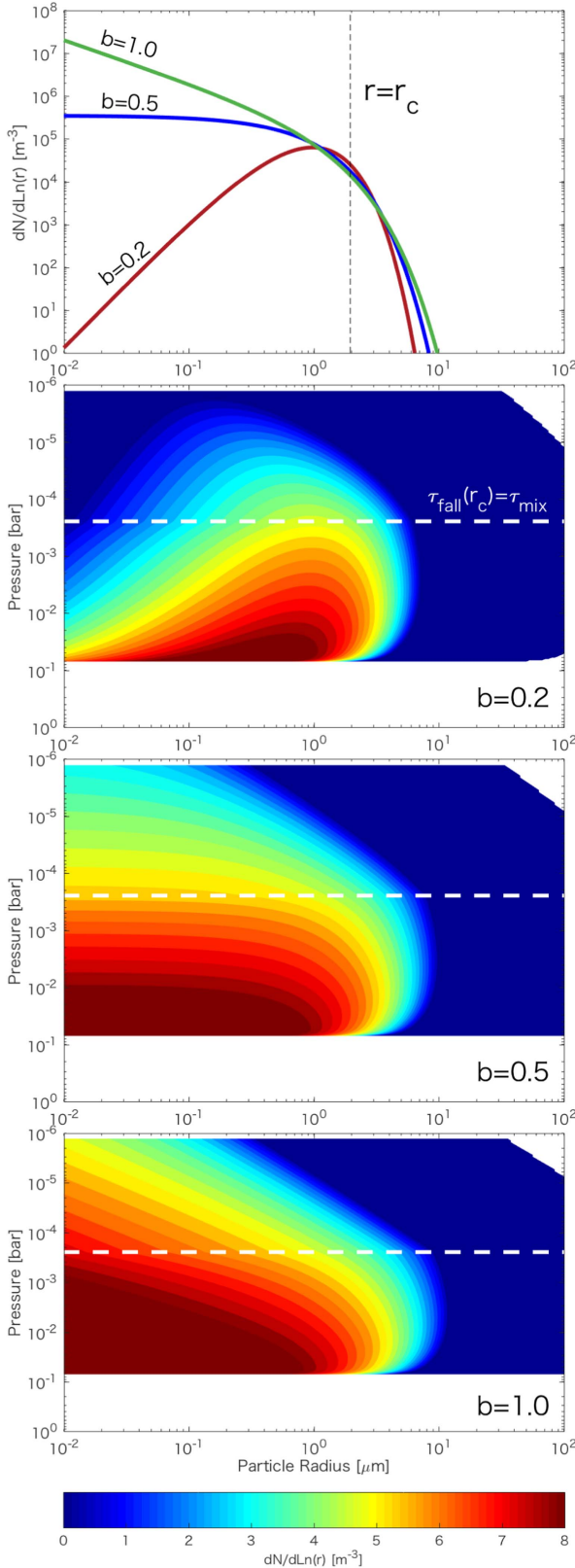


Figure 8. Constructed particle size distributions. The metallicity of $100\times$ solar and $N_{\text{CCN}} = 10^9 \text{ m}^{-3}$ are selected. The top panel shows the size distributions for $b = 0.1, 0.5$, and 1.0 at the height where $\tau_{\text{mix}} = \tau_{\text{fall}}(r_c)$, denoted as white dotted lines in lower panels. Each panel, from second to bottom, shows the vertical size distributions for $b = 0.1, 0.5$, and 1.0 , respectively.

Figure 5 shows that the final particle size asymptotically reaches that predicted from Equation (27), except in the case of steam atmosphere. The deviation for steam atmosphere is caused by coalescence, as explained in next subsection.

3.2.3. Enriched Vapor Regime ($\tau_{\text{coal}} < \tau_{\text{mix}}$)

Coalescence is dominant only if condensing vapor is very abundant as in pure steam atmospheres, as shown in the right panel of Figure 4. When coalescence is dominant, the final particle size becomes larger than the lower limit set by coagulation r_{coag} (see the bottom panel of Figure 5). Because larger particles have larger settling velocity, coalescence suppresses the cloud-top height in the steam atmosphere.

Here we predict the threshold abundance of condensing vapor that induces the significant growth through coalescence. Because the particle size is smaller than the gas mean free path near the cloud base $\sim 10 \mu\text{m}$ in most of our calculations, the terminal velocity is expressed as the Epstein's law, approximated as

$$v_t(r_c) \approx \frac{2\beta_\infty g \rho_p}{3\rho_g v_{\text{th}}} r_c. \quad (28)$$

Therefore the coalescence timescale can be rewritten as

$$\begin{aligned} \tau_{\text{coal}} &= \frac{1}{2\pi r^2 \Delta v n} \\ &= \frac{2v_{\text{th}}}{\beta_\infty g q_c}. \end{aligned} \quad (29)$$

Because $q_c = m_{\text{KCl}} q_{\text{KCl}} / m_g$ (see Section 3.2.2), the coalescence timescale just above the cloud base is independent of n_{CCN} , and only depends on the mixing ratio of the condensing vapor. If $\tau_{\text{coal}} \ll \tau_{\text{mix}}$, the cloud particles grow via coalescence in addition to condensation and coagulation. Comparing Equation (29) with $\tau_{\text{mix}}(z_b)$, we find that coalescence occurs near the cloud base if the condensate mixing ratio is much higher than

$$\begin{aligned} q_* &\approx \frac{2v_{\text{th}} K_z m_g}{\beta_\infty g H^2 m_{\text{KCl}}} \\ &\approx 5 \times 10^{-7} \left(\frac{g}{10 \text{ m s}^{-2}} \right)^{-1/2} \left(\frac{H}{10^2 \text{ km}} \right)^{-3/2} \\ &\quad \times \left(\frac{K_z(z_b)}{10^3 \text{ m}^2 \text{ s}^{-1}} \right) \left(\frac{m_g}{2 \text{ amu}} \right). \end{aligned} \quad (30)$$

Substituting the parameters for the steam atmosphere of GJ1214 b, the mixing ratio of condensing vapor $q_{\text{KCl}} = 2.61 \times 10^{-4}$ exceeds the $q_* \sim 2 \times 10^{-5}$ by an order of magnitude, and hence coalescence dominates the particle growth.

3.3. Predicting the Maximum Cloud-top Height

The prediction of the cloud-top height, defined as the height at which the atmosphere becomes opaque due to the cloud, is important because it determines the shape of observed spectra (e.g., Brown 2001). In order to predict it, we calculate the slant optical depth τ_s , defined as the optical depth for the path length of the transmitted starlight, using Equation (6) of Fortney

(2005), given by

$$\tau_s = \tau_v \sqrt{\frac{2\pi R_p}{H_c}}, \quad (31)$$

where τ_v is the vertical optical depth of the cloud, R_p is the planetary radius, and $H_c = |d \ln n_c / dz|^{-1}$ is the cloud scale height. The cloud-top height can be estimated as the height at which τ_s exceeds unity. The vertical optical depth τ_v is given by

$$\tau_v(z) = \int_z^\infty Q_{\text{ext}}(r_c) \pi r_c^2 n_c dz, \quad (32)$$

where Q_{ext} is the extinction coefficient of the particles. To calculate Q_{ext} , we perform rigorous Mie calculations using *BHME* code (Bohren & Huffman 1983). We use the refractive index of KCl from Querry (1987) and assume an isotropic scattering for the calculations of scattering opacities. We assume the wavelength of $\lambda = 1.4 \mu\text{m}$, at which a prominent water feature is located. For GJ1214 b and GJ436 b, this feature is absent in the actual spectra (Knutson et al. 2014a; Kreidberg et al. 2014), and therefore the cloud-top height defined at $1.4 \mu\text{m}$ must be sufficiently high so that the clouds fully obscure the feature.

To estimate H_c , we use the fact that at high altitudes particle growth is negligible, and hence the vertical profiles are given by Equation (18). Since $H = |d \ln n_g / dz|^{-1}$ and $H_c = |d \ln n_c / dz|^{-1}$, Equation (18) can be rewritten as

$$H_c = H \left(1 + \frac{v_t H}{K_z} \right)^{-1}. \quad (33)$$

Because the term $v_t H / K_z$ is the ratio of τ_{mix} to τ_{fall} , $H_c \approx H$ for $\tau_{\text{mix}} \ll \tau_{\text{fall}}$, and $H_c \approx K_z / v_t$ for $\tau_{\text{mix}} \gg \tau_{\text{fall}}$.

Figure 6 shows the cloud-top pressure for GJ1214 b predicted by our calculations for different values of the metallicity and n_{CCN} . We find that the cloud-top height increases with n_{CCN} , but plateaus in the limit of high n_{CCN} . This means that one can predict the maximum height of the cloud top for given atmospheric metallicity. The presence of the maximum height results from the presence of the minimum particle size mentioned in Section 3.2.2. The impact of size distribution on the predicted maximum height is small, as we will discuss in Section 5.1.

We also find that metal-enriched atmospheres are more likely to yield vertically extended clouds for the abundance of condensing vapor below the threshold (Equation (30)). Figure 6 shows that the cloud-top is placed at $P \gtrsim 3 \times 10^{-3}$ bar for $1 \times$ solar metallicity, $P \gtrsim 3 \times 10^{-4}$ bar for $10 \times$ solar metallicity, $P \gtrsim 1 \times 10^{-4}$ bar for $100 \times$ solar metallicity, and $P \gtrsim 6 \times 10^{-4}$ bar for the steam atmosphere. This trend arises because a higher metallicity atmosphere yields a higher total cloud mass and more efficient vertical mixing as mentioned before. For vapor abundance above the threshold, the case of the steam atmosphere, cloud-top height no longer increases with metallicities because coalescence leads significant growth for cloud particles, as mentioned in Section 3.2.3.

4. Application to GJ1214 b and GJ436 b

Now we apply our cloud model to two super-Earths, GJ1214 b and GJ436 b, which are known to exhibit a flat transmission spectrum. As mentioned in the previous section, there is a maximum height, or equivalently a minimum atmospheric pressure P_{min} , that can be reached by the top of a KCl cloud for given atmospheric metallicity. In order to

Table 3
Maximum Cloud-top Height for Different P–T Structures

Metallicity	Charnay et al. (2015a)	Guillot (2010)
$1 \times$ solar	$P_{\text{min}} = 3.6 \times 10^{-3}$ bar	$P_{\text{min}} = 3.5 \times 10^{-3}$ bar
$10 \times$ solar	$P_{\text{min}} = 4.7 \times 10^{-4}$ bar	$P_{\text{min}} = 3.8 \times 10^{-4}$ bar
$100 \times$ solar	$P_{\text{min}} = 1.4 \times 10^{-4}$ bar	$P_{\text{min}} = 1.2 \times 10^{-5}$ bar
Steam	$P_{\text{min}} = 1.2 \times 10^{-3}$ bar	$P_{\text{min}} = 6.2 \times 10^{-4}$ bar

examine whether KCl clouds are responsible for the flat transmission spectra, we compare the maximum cloud-top heights with the cloud heights observationally inferred for the two super-Earths.

4.1. GJ1214 b

In the left panel of Figure 7, we plot the height (in pressure) of the cloud base and the maximum height of the cloud top predicted for GJ1214 b as a function of the metal mass fraction of the atmosphere.³ The blue-shaded area in Figure 7 thus indicates the heights where the top of the KCl cloud can exist for some CCN number density. For comparison, we also indicate by the gray shading the heights of the cloud top suggested by Kreidberg et al. (2014), based on Bayesian analysis on the observed transmission spectrum.

We find that the maximum cloud-top height is too low to explain the flat spectrum for all plausible values of the atmospheric metallicity. In principle, a higher atmospheric metallicity provides a higher cloud-top height, as already mentioned in Section 3.3. However, even if we assume the steam atmosphere, the maximum cloud-top height ($P_{\text{min}} = 6 \times 10^{-4}$ bar in pressure) is still an order of magnitude higher than inferred by Kreidberg et al. (2014; cloud-top pressure $\leq 3 \times 10^{-5}$ bar at 3σ confidence). This is because in the steam atmosphere, coalescence causes the significant growth of cloud particles of $r_c \geq 5 \mu\text{m}$.

The above comparison clearly shows that a simple condensate cloud cannot explain the flat transmission spectrum of GJ1214 b. This fact might support the idea that the flat spectrum of GJ1214 b is caused by photochemical haze (Miller-Ricci Kempton et al. 2012; Morley et al. 2013, 2015; Kawashima & Ikoma 2018), rather than by mineral clouds. Alternatively, our cloud model might still be missing important physics of particle growth. For example, it is suggested both theoretically and experimentally (e.g., Dominik & Tielens 1997; Blum & Wurm 2000) that, unlike water cloud droplets, solid particles grow into highly porous particles through mutual sticking. This porosity evolution is neglected in Figure 7, but could help particles ascend to very high altitudes because porous particles have a lower settling velocity than compact particles of the same mass. We address this possibility in Section 5.3.

4.2. GJ436 b

For GJ436 b, we find that the maximum cloud-top height for KCl clouds is high enough to be consistent with the transmission observations. The Bayesian analysis by Knutson et al. (2014a) indicates that the cloud top is present at atmospheric pressures of $\lesssim 10^{-2}$ bar, except for metal-rich atmospheres of metal mass

³ Metal mass fraction is defined as the mass fraction of heavy element. Following Fortney et al. (2013), we calculate metal mass fraction assuming H–He–water mixtures in this study.

fraction $\gtrsim 0.8$, for which the location of the cloud top is not well constrained (see the gray-shaded area in the right panel of Figure 7). As shown in the right panel of Figure 7, the minimum cloud-top pressure P_{\min} predicted from our model is 2×10^{-3} , 3×10^{-4} , 8×10^{-5} , and 5×10^{-6} bar for the metallicities of $1\times$, $10\times$, $100\times$, and $1000\times$ solar, respectively. Since we adopted the high K_z for the metallicity of $1000\times$ solar compared with that for the steam atmosphere on GJ1214 b, cloud particles avoid the significant growth due to coalescence. This is a reason why the cloud-top height for $1000\times$ solar is much higher than that for the steam atmospheres on GJ1214 b. Combining the Bayesian analysis results and our model prediction, we suggest that the flat spectrum of GJ436 b is likely caused by a KCl cloud with its top at $\sim 10^{-3}$ – 10^{-2} bar for hydrogen-rich atmospheres (metal mass fraction $\lesssim 0.8$) and at $\sim 10^{-2}$ – 10^{-5} bar for metal-rich atmospheres (metal mass fraction $\gtrsim 0.8$). However, because we here adopted a metallicity-independent eddy diffusion coefficient (see Section 2.3), we cannot conclude whether the atmosphere of GJ436 b is likely to be hydrogen-rich or metal-rich. Future three-dimensional modeling of GJ436 b's atmospheric circulation, like the one done by Charnay et al. (2015a) for GJ1214 b, would allow us to determine the atmosphere's metallicity.

5. Discussion

5.1. Influences of Size Distribution on the Cloud-top Height

Because the total particle cross section tends to be dominated by small particles rather than by the particles dominating the total cloud mass, the cloud-top height might be influenced by the size distribution, which is, however, not captured by our calculations. We here evaluate the impact of particle size distribution on the predicted cloud-top height by adding to our model a distribution of small particles. We assume that particles smaller than r_c obey the Hansen size distribution (Hansen 1971) given by

$$f(r) \equiv \frac{dn}{dr} = Cr^{(1-3b)/b} \exp\left(-\frac{r}{ab}\right), \quad (34)$$

where $f(r)dr$ is the number density of particles with radii between r and $r + dr$, C is a constant, a and b are the mean effective radius, and the effective variance defined by

$$a \equiv \frac{\int_0^\infty r\pi r^2 f(r) dr}{\int_0^\infty \pi r^2 f(r) dr}, \quad (35)$$

$$b \equiv \frac{\int_0^\infty (r - a)^2 \pi r^2 f(r) dr}{a^2 \int_0^\infty \pi r^2 f(r) dr}. \quad (36)$$

The Hansen size distribution successfully reproduces the observed size distributions of terrestrial water clouds for $b = 0.1$ – 0.2 (Hansen 1971), and near-infrared spectral energy distributions of cloudy brown dwarfs for $b > 0.5$ (Hiranaka et al. 2016). The top panel of Figure 8 shows the Hansen size distributions for $b = 0.2$, 0.5 , and 1.0 . One can see that $b < 0.5$ yields log-normal-like size distributions, while $b > 0.5$ yields power-law-like size distributions. Therefore, the Hansen size distribution with various choices of b enables us to test the size distributions of various shapes.

For each height, we determine the a and C so that the mass weighted size and the cloud mass density correspond to r_c and ρ_c calculated by our model, respectively. We calculate the a

and C at each height using the following relations:

$$r_c = \frac{\int_0^\infty r m(r) f(r) dr}{\int_0^\infty m(r) f(r) dr} = a(1 + b), \quad (37)$$

$$\rho_c = \frac{4\pi\rho_p}{3} C (ab)^{(1+b)/b} \Gamma\left(\frac{1+b}{b}\right), \quad (38)$$

where $\Gamma(z)$ is the gamma function. However, r_c might be overestimated in our calculations at the height where $\tau_{\text{mix}} > \tau_{\text{fall}}(r_c)$, because our model fails to trace the decreasing of mass weighted size due to the removal of large particles by gravitational settling. To avoid this issue, we use an analytical solution of the transport equation. In the upper atmosphere, the particle growth is negligible, as mentioned in Section 3, and hence, in a steady state, the particle number density obeys

$$-n_g K_z \frac{\partial}{\partial z} \left(\frac{n_c}{n_g} \right) - v_t n_c = 0. \quad (39)$$

If we approximate $\beta = 1 + \beta_\infty \text{Kn}_g$,⁴ Equation (39) can be analytically solved as

$$\begin{aligned} n_c(P) &= n_c(P_0) \mathcal{P} \\ &\times \exp \left[\frac{5\chi(P_0)}{2(1 + \beta_\infty \text{Kn}_0)} \right] \\ &\times \left(\left(\mathcal{P}^{2/5} - 1 \right) - \frac{2\beta_\infty \text{Kn}_0}{3} (\mathcal{P}^{-3/5} - 1) \right), \end{aligned} \quad (40)$$

where $\mathcal{P} \equiv P/P_0$ and $\chi(P) \equiv \tau_{\text{mix}}(P)/\tau_{\text{fall}}(P)$ is the ratio of the mixing timescale to the falling timescale. We calculate the size distributions at the regions of $\tau_{\text{mix}} < \tau_{\text{fall}}(r_c)$ using Equation (40) for each size bin. Figure 8 shows the constructed vertical size distributions for $b = 0.2$, 0.5 , and 1.0 . The reference pressure P_0 is set as a height where $\tau_{\text{mix}} = \tau_{\text{fall}}(r_c)$, denoted as the white dotted lines in each panel. Figure 8 indicates that the larger b is, the more small particles are present at high altitude.

Figure 9 compares the cloud-top heights predicted by the characteristic size model with those by the model with the Hansen size distribution of $b = 0.2$, 0.5 , and 1.0 . With particle size distribution, the vertical optical depth is calculated as

$$\tau_v(z) = \int_z^\infty \int_0^\infty Q_{\text{ext}}(r) \pi r^2 f(r, z) dr dz. \quad (41)$$

We find that size distribution has little effect on the cloud top height, except for the case of the steam atmosphere. This is because KCl is a purely scattering material in near-infrared (i.e., the extinction is equivalent to the scattering). For purely scattering particles smaller than the wavelength, the extinction efficiencies steeply decrease with decreasing the particle size as $Q_{\text{ext}} \propto r^4$. Therefore, the contribution of such small particles ($r \ll \lambda$) to the total cloud opacity is negligibly small. The most efficient extinction occurs at $r \sim \lambda/2\pi$, which is $0.2 \mu\text{m}$ for $\lambda = 1.4 \mu\text{m}$. By contrast, the final characteristic sizes for the metallicities of $1\times$, $10\times$, and $100\times$ solar are $r_c \approx 1 \mu\text{m}$ (see

⁴ This expression asymptotically approaches Equation (8) in the limits of small and large Kn_g . The maximum deviation from Equation (8) is only $\approx 10\%$, which occurs at $\text{Kn}_g = 1$.

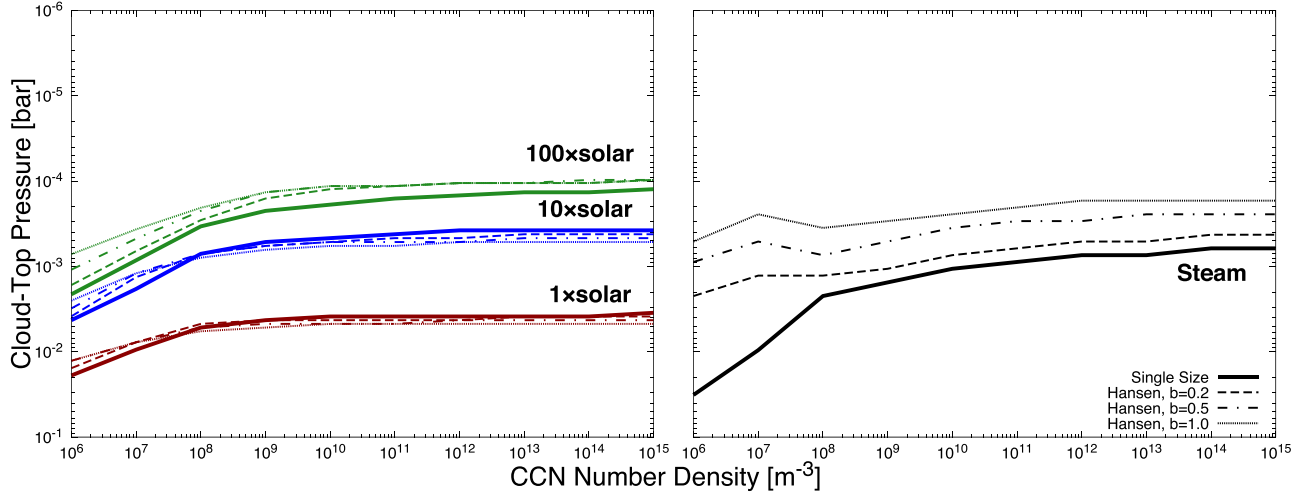


Figure 9. Cloud-top pressures as a function of CCN number density for hydrogen-rich atmosphere models (left panel) and the steam atmosphere model (right panel), obtained from models of different particle size distribution. The red, blue, green, and black lines are for 1×, 10×, 100× solar models, and pure steam atmosphere, respectively. The solid lines are calculated for characteristic size method, while the dashed lines, dashed dotted lines, and dotted lines are calculated for the Hansen size distribution with $b = 0.2, 0.5$, and 1.0 , respectively.

Figure 5), already close to $0.2 \mu\text{m}$. Therefore, the addition of particles smaller than r_c has little effect on the optical depth and hence on the cloud-top height.

The difference arising from size distributions becomes obvious only when the final characteristic size is orders of magnitude larger than $r = \lambda/2\pi$. This is the case for the steam atmospheres, in which the final characteristic size is $r \approx 5 \mu\text{m} \gg 0.2 \mu\text{m}$. In this case, varying the size distribution can decrease the cloud-top pressure by a factor of 3 from the prediction of the characteristic size method. However, we find that the cloud-top height for GJ1214 b with a steam atmosphere is still an order of magnitude lower than anticipated from the observation of Kreidberg et al. (2014). Thus we conclude that one cannot explain the flat spectrum of GJ1214 b solely by considering particle size distribution.

5.2. Influences of the Convective Adjustment

Our P–T structure neglects heat transport by convection, which is the process called “convective adjustment,” and in reality becomes important when the temperature steeply declines with decreasing pressure (Manabe & Strickler 1964; Marley & Robinson 2015). We performed test calculations using the P–T structure provided by Charnay et al. (2015a), which includes the effect of the convective adjustment. As listed in Table 3, we confirmed that the maximum heights of cloud top are quantitatively similar to the results from radiative P–T profiles of Guillot (2010). The largest influence is only a factor of 2, which occurs for the case of the steam atmospheres. The reason why the cloud-top height is nearly the same for both P–T structures is that the convective adjustment only changes the cloud-base height slightly. Since the minimum particle size is not sensitive to the cloud-base height ($r_{\text{coag}} \propto P_b^{1/10}$ from Equation (27)), the convective adjustment has little effect on the predicted cloud-top height.

5.3. Cloud-top Height for Porous Cloud Particles

In the calculations presented in Sections 3 and 4, we assumed that cloud particles are compact and their internal density is constant. This assumption would be valid for liquid

droplets, but breaks down if solid KCl cloud particles grow into porous aggregates. As pointed out by Marley et al. (2013), porous aggregates are easily lofted to high altitude because they have large cross sections as compared with compact particles of the same mass. Therefore, the predicted cloud-top height could be influenced by particle porosity.

Here we quantify the impacts of particle porosity on the predicted cloud-top height. We introduce the volume filling factor ϕ defined by

$$\phi \equiv \frac{\rho_{\text{int}}}{\rho_p}. \quad (42)$$

The volume filling factor takes $\phi = 1$ for compact particles and $\phi < 1$ for porous particles. Snowflakes in the Earth are known to have $\phi = 0.5\text{--}0.005$ (Magono & Nakamura 1965), while grains in protoplanetary disks could have an extremely low filling factor of $\phi \sim 10^{-4}$ according to recent theoretical studies (Okuzumi et al. 2012; Kataoka et al. 2013). We repeat the calculations presented in Section 3.3 by replacing ρ_p as ρ_{int} and varying ϕ from $\phi = 1$ to $\phi = 0.01$.

To evaluate Q_{ext} for porous aggregates, we calculate the effective refractive index using the effective medium theory (EMT) with the Maxwell-Garnett mixing rule (Bohren & Huffman 1983). The EMT provides reasonable estimates for aggregate’s absorption and scattering opacities when the particles that constitute the aggregates are smaller than the incident wavelength (Voshchinnikov et al. 2007; Shen et al. 2008).

In Figure 10, we show the final characteristic size and cloud-top height for various values of ϕ and atmospheric metallicities. We find that the final characteristic size increases with decreasing ϕ . This is because, in the limit of high N_{CCN} , the final characteristic size is proportional to $\phi^{-1/4}$ as indicated by Equation (26). Since $v_i \propto \rho_p r_c \propto \phi^{3/4}$ in upper atmospheres (see Equation (28)), porous aggregates are indeed easily lofted to high altitude as compared with compact particles.

However, the cloud-top height does not appreciably increase with decreasing ϕ except for the steam atmosphere (see each bottom panel of Figure 10). When the particle porosity is taken into account, the maximum cloud-top height is $\sim 2 \times 10^{-3}$ bar

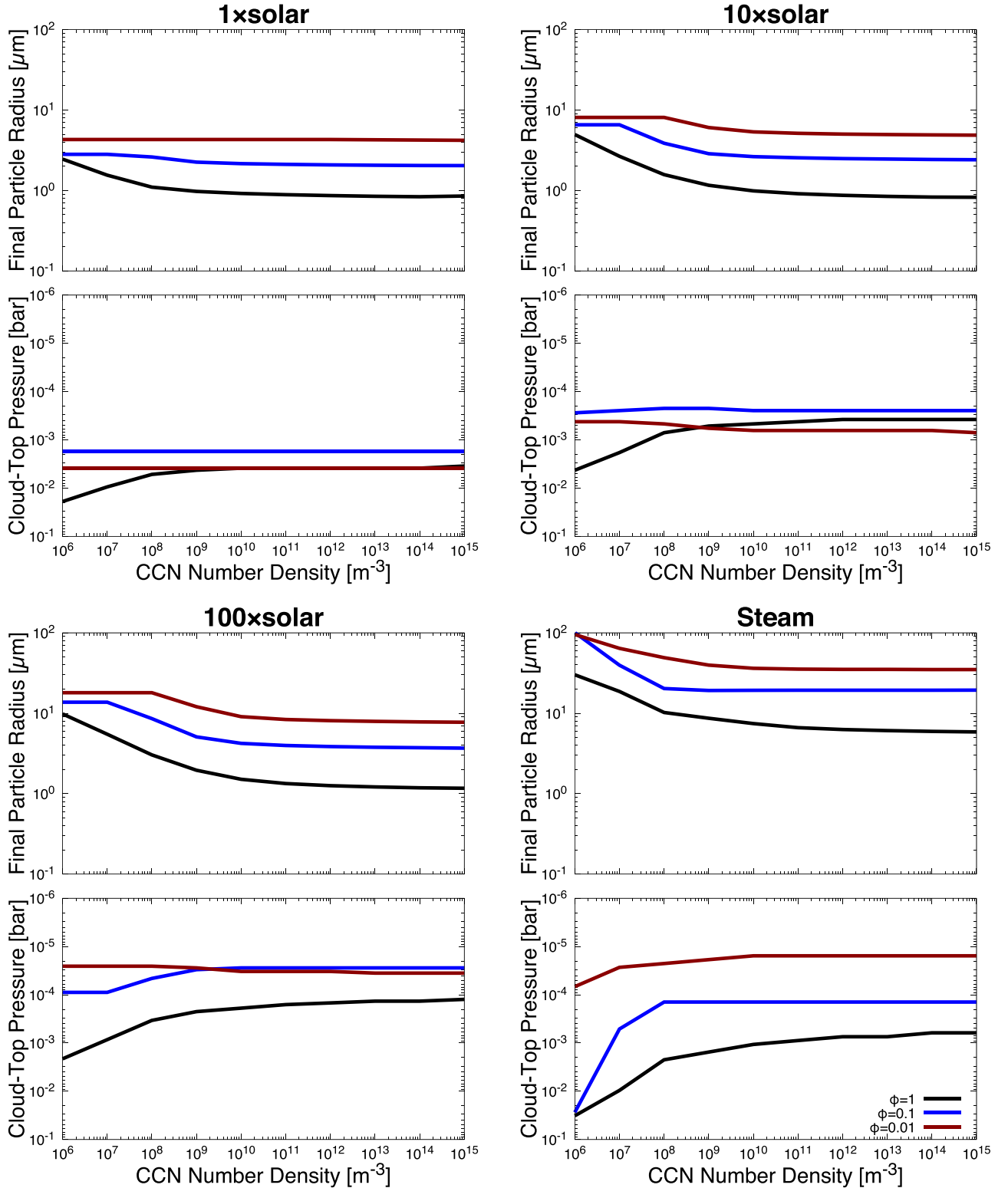


Figure 10. Cloud-top pressures for various volume filling factors and atmospheric metallicities. The black, red, and blue lines denote the results for $\phi = 1$, 0.1, and 0.01, respectively. The top and bottom panels of each block show the final particle radius and cloud-top pressure for different atmospheric metallicities.

for the metallicity of $1 \times$ solar, $\sim 2 \times 10^{-4}$ bar for $10 \times$ solar, and $\sim 3 \times 10^{-5}$ bar for $100 \times$ solar, respectively, which are only higher than those for compact particles by a factor of 2–3. The reason why the cloud-top height is insensitive to ϕ comes from the optical properties of porous aggregates, shown in

Figure 11. The scattering mass opacity of a porous aggregate is proportional to ϕ as long as $\phi < \lambda/r$, in which the aggregate itself becomes optically thin (Kataoka et al. 2014). The two effects of reducing opacities and increasing the cloud amounts at high altitude with decreasing ϕ largely cancel out, explaining

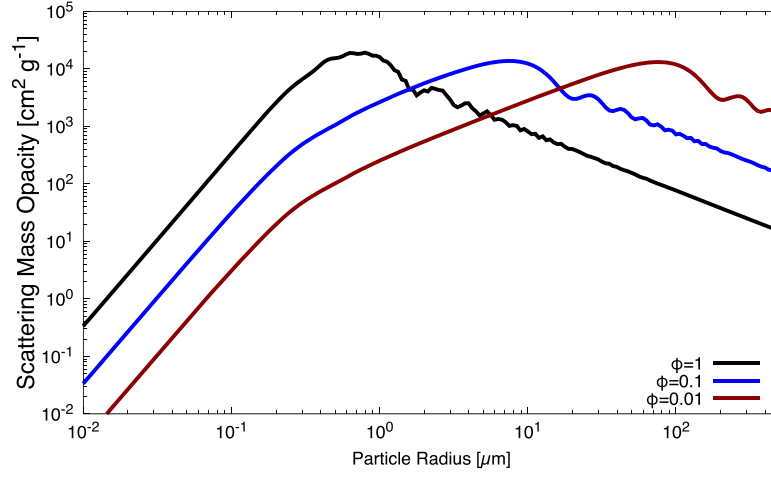


Figure 11. Scattering mass opacity for porous aggregates as a function of particle size calculated by Mie theory instrumented with EMT. The color differences denote the differences in ϕ . The wavelength is set as $\lambda = 1.4 \mu\text{m}$.

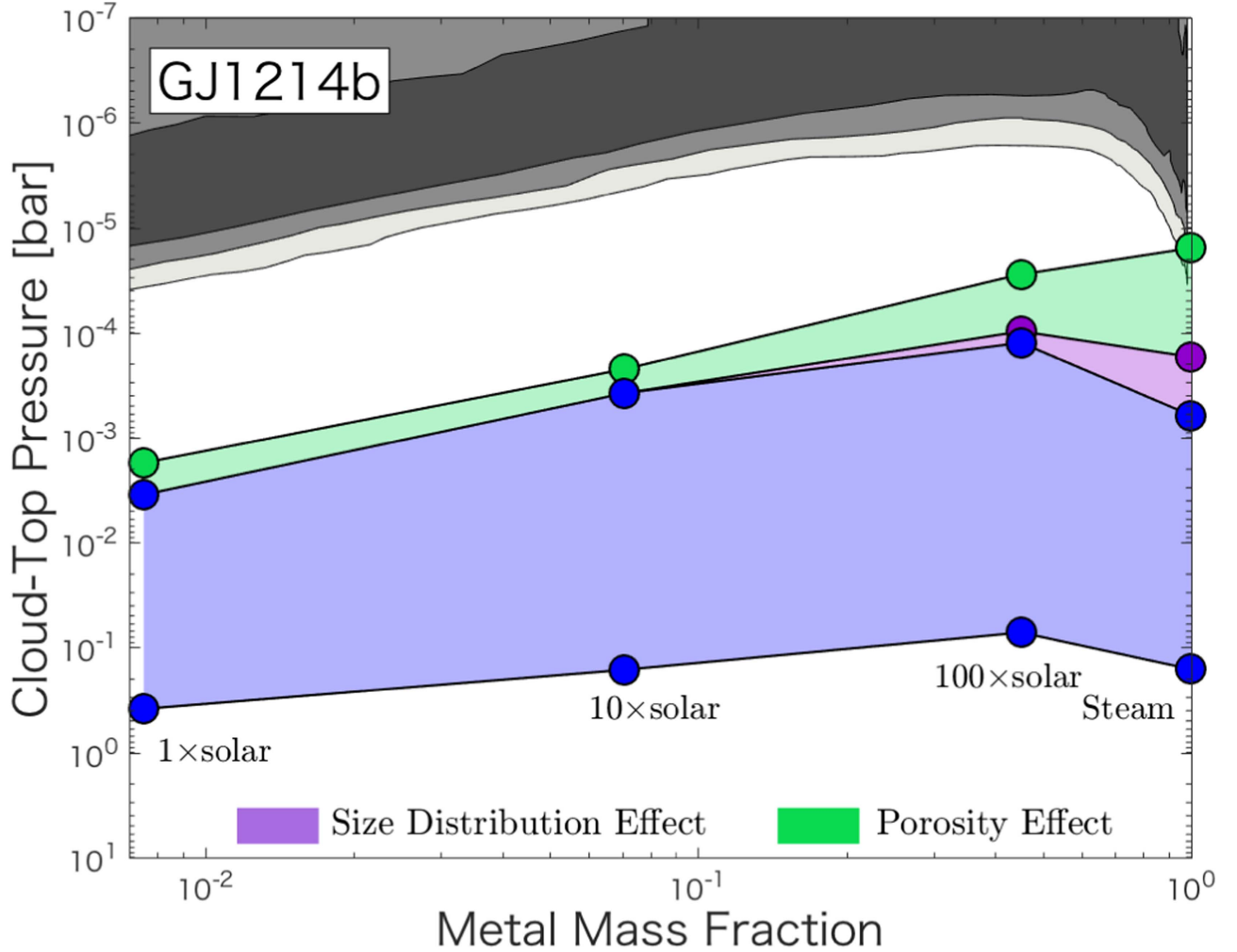


Figure 12. Same as the left panel of Figure 7, but from models including the effects of size distribution (purple shaded area) and particle porosity (green shaded area).

why the impacts of particle porosities are not drastic for hydrogen-rich atmospheres.

By contrast, for the steam atmosphere, the cloud-top height for porous aggregates can be much higher than that for compact

particles. The maximum cloud-top height is $\sim 1 \times 10^{-4}$ bar for $\phi = 0.1$ and $\sim 2 \times 10^{-5}$ bar for $\phi = 0.01$. The distinct increase in cloud-top height is caused by the efficient growth via coalescence. Because τ_{coal} only depends on the cloud mass

mixing ratio (see Equation (29)), the efficient growth via coalescence occurs even for porous aggregates. Coalescence produces particles large enough to have a high scattering opacity, and hence the cancellation due to the effect of reducing opacities with decreasing ϕ does not occur appreciably. This is a reason why the particle porosity drastically increases the cloud-top height for the steam atmosphere.

Figure 12 shows the maximum extent of KCl clouds for GJ1214 b from the models that take into account size distribution (Section 5.1) and particle porosity. We find that the cloud-top height is still too low to be consistent with the flat spectrum of Kreidberg et al. (2014) for hydrogen-rich atmospheres ($1\times$, $10\times$, and $100\times$ solar metallicities). On the other hand, for the steam atmosphere with $\phi = 0.01$, we find that KCl clouds can reach $\approx 1.5 \times 10^{-5}$ bar, which is equivalent to within the 3σ Bayesian credible regions of the cloud-top height ($P \approx 3 \times 10^{-5}$ bar) reported by Kreidberg et al. (2014). Since particle porosity naturally increases through coalescence, high-altitude cloud formation in the steam atmospheres, where coalescence is effective, might be a plausible explanation for the flat spectrum of GJ1214 b.

We note that the estimates for the cloud-top height given above are based on the assumption of isotropic scattering. The forward scattering of cloud particles potentially reduces the effective cloud opacity (de Kok & Stam 2012; Robinson 2017) and hence produces a lower cloud top. This effect cannot be captured here correctly because EMT tends to overestimate the degree of forward scattering of porous aggregates (Shen et al. 2009; Tazaki et al. 2016; Tazaki & Tanaka 2018). The angular dependent properties of scattered light depend on the microstructure of an aggregate. Further understanding about the microstructure and optical property of aggregates is required to verify the possibility of high-altitude cloud formation by porous aggregates.

6. Conclusions

We have investigated how the vertical profiles of mineral clouds in super-Earths vary with the atmospheric metallicity and CCN concentration. We used a cloud microphysical model that takes into account the condensation, collision growth, and vertical transport of mineral particles in a self-consistent manner. We have discussed how the particle size is determined by microphysical processes, and compared the predicted cloud profiles with the observations of GJ1214 b and GJ436 b. Our main findings are summarized as follows.

1. The vertical profiles of mineral clouds significantly vary with CCN concentration and atmospheric metallicity. The particle size decreases with increasing CCN concentration, and increases with increasing metallicity. The cloud particle's size is always larger than the minimum size determined by coagulation growth at high altitude (Equation (26)). When the mixing ratio of condensing vapor exceeds a threshold, the cloud particles grow further through coalescence.
2. Particle growth through coagulation and coalescence sets the maximum height that can be reached by a mineral cloud. When the mixing ratio of condensing vapor is lower than a threshold (Equation (30)), the maximum cloud-top height is set by coagulation and increases with increasing metallicity. For mixing ratios above the threshold, the cloud-top height no longer increases with

metallicity, because coalescence causes further growth of the particles.

3. For GJ436 b, we have found that mineral clouds can ascend to the height suggested from the transmission spectrum (Knutson et al. 2014a) for all ranges of metallicity ($1\text{--}1000\times$ solar). Since we adopted a metallicity-independent eddy diffusion coefficient, future investigation on its metallicity dependence will allow us to determine the plausible atmospheric metallicity of GJ436 b.
4. For GJ1214 b, our model suggests that KCl clouds cannot reach the height where the presence of a cloud has been inferred from the transmission spectrum (Kreidberg et al. 2014). Previous cloud models suggested high-altitude clouds can form in GJ1214 b if the atmosphere's metallicity is higher than $100\times$ solar and if the cloud particle radius is around $0.5\text{ }\mu\text{m}$ (Charnay et al. 2015a, 2015b). However, we have found that the particles always grow beyond a micron in radius through coalescence and coagulation, and suffer from ascending high enough height to explain transmission observations. Even if the size distribution is taken into account, the height of KCl clouds is too low to be consistent with the observation of GJ1214 b, because the mass-dominating particles, which are treated in our model, also dominate the total opacity in near-infrared for these particular examples.
5. Porosity evolution of cloud particles might explain the presence of the high-altitude cloud in GJ1214 b. We have found that KCl clouds can reach the height suggested by Kreidberg et al. (2014) if the cloud particles have a filling factor of 0.01 and if the atmosphere is extremely metal-enriched. Since metal-enriched atmospheres lead to coalescence that naturally yields porous aggregates, this possibility might be a plausible solution for the flat transmission spectrum of GJ1214 b. Our future modeling of the microstructure and optical properties of porous aggregates will pursue this possibility.

The authors thank the anonymous referee for insightful comments that greatly improved this paper. We also thank Peter Gao and Diana Powell for providing paper manuscripts, and Shigeru Ida, Hidekazu Tanaka, Xi Zhang, Chris Ormel, Ryo Tazaki, Yamira Miguel, Masahiro Ogihara, Yuichi Ito, and Yui Kawashima for helpful comments. This work was supported by JSPS Grants-in-Aid for Scientific Research (#15H02065, 16H04081, 16K17661, 18J14557) and the Foundation for Promotion of Astronomy.

Appendix Evaluation of Physical Quantities

Here we summarize the evaluation of each physical quantity used in our calculations.

For hydrogen-rich atmosphere (metallicity of $1\times$, $10\times$, and $100\times$ solar), we adopted the convenient formula of kinetic viscosity η , mean free path l , and thermal conductivity K proposed by Woitke & Helling (2003):

$$\eta = 5.877 \times 10^{-7} \text{ Pa s } \sqrt{T[\text{K}]}, \quad (43)$$

$$l = 1.86 \times 10^{-6} \text{ m} \left(\frac{\rho_g}{10^{-2} \text{ kg m}^{-3}} \right)^{-1}, \quad (44)$$

$$K = 988 \times 10^{-5} \text{ W K}^{-1} \text{ m}^{-1} \sqrt{T[\text{K}]}. \quad (45)$$

For metal-rich cases (steam atmosphere and $1000\times$ solar), we adopted the original formula of kinetic viscosity—that is,

$$\eta = \Sigma_i \frac{0.499 n_i m_i v_i^{\text{th}}}{\Sigma n_j \pi (r_i + r_j)^2 \sqrt{1 + m_i/m_j}}, \quad (46)$$

where n_i , m_i , r_i , and $v_i^{\text{th}} = \sqrt{8k_B T / \pi m_i}$ are the number densities, mass, radius, and thermal velocity of gas particles i , respectively. In accordance with Woitke & Helling (2003), we used the radii of hydrogen $r_{\text{H}_2} = 1.36 \text{ \AA}$ and $r_{\text{He}} = 1.09 \text{ \AA}$. For the water, we adopted the molecular diameter used by Charnay et al. (2015a), given by

$$d_{\text{H}_2\text{O}} = 4.597 \text{ \AA} \left(\frac{T}{300 \text{ K}} \right)^{-0.3}. \quad (47)$$

We also calculated the mean free path from the relation of $\eta = \rho_g \bar{v}_{\text{th}} l / 3$, where $\bar{v}_{\text{th}} = \sqrt{8k_B T / \pi m_g}$. In accordance with Woitke & Helling (2003), we also calculated the thermal conductivity as

$$K = \frac{9\gamma - 5}{4} \eta C_V, \quad (48)$$

where γ is the heat capacity ratio.

The diffusivity of vapor in the atmosphere is required to calculate the condensation growth. The molecular diffusion coefficient for species i is given by Jacobson (2005) as

$$D = \frac{5}{16 N_A d_i^2 \rho_g} \sqrt{\frac{RT m_g}{2\pi} \left(\frac{m_i + m_g}{m_i} \right)}, \quad (49)$$

where N_A is Avogadro's number and d_i is the collision diameter. We took the collision diameter of KCl molecules from equilibrium bond length, $d_{\text{KCl}} = 2.67 \text{ \AA}$ (Lovas & Tiemann 1974).

ORCID iDs

Satoshi Okuzumi  <https://orcid.org/0000-0002-1886-0880>

References

- Ackerman, A. S., & Marley, M. S. 2001, *ApJ*, **556**, 872
- Bean, J. L., Miller-Ricci Kempton, E., & Homeier, D. 2010, *Natur*, **468**, 669
- Berta, Z. K., Charbonneau, D., Désert, J.-M., et al. 2012, *ApJ*, **747**, 35
- Birnstiel, T., Klahr, H., & Ercolano, B. 2012, *A&A*, **539**, A148
- Blum, J., & Wurm, G. 2000, *Icar*, **143**, 138
- Bohren, C. F., & Huffman, D. R. 1983, *Absorption and Scattering of Light by Small Particles* (New York: Wiley)
- Brauer, F., Dullemond, C. P., & Henning, T. 2008, *A&A*, **480**, 859
- Brown, T. M. 2001, *ApJ*, **553**, 1006
- Charnay, B., Meadows, V., & Leconte, J. 2015a, *ApJ*, **813**, 15
- Charnay, B., Meadows, V., Misra, A., Leconte, J., & Arney, G. 2015b, *ApJL*, **813**, L1
- Davies, C. N. 1945, *PPS*, **57**, 259
- de Kok, R. J., & Stam, D. M. 2012, *Icar*, **221**, 517
- Domink, C., & Tielens, A. G. G. M. 1997, *ApJ*, **480**, 647
- Dragomir, D., Benneke, B., Pearson, K. A., et al. 2015, *ApJ*, **814**, 102
- Ehrenreich, D., Bonfils, X., Lovis, C., et al. 2014, *A&A*, **570**, A89
- Ferrier, B. S. 1994, *JatS*, **51**, 249
- Fortney, J. J. 2005, *MNRAS*, **364**, 649
- Fortney, J. J., Mordasini, C., Nettelmann, N., et al. 2013, *ApJ*, **775**, 80
- Fraine, J., Deming, D., Benneke, B., et al. 2014, *Natur*, **513**, 526
- Freedman, R. S., Lustig-Yaeger, J., Fortney, J. J., et al. 2014, *ApJS*, **214**, 25
- Gao, P., Marley, M. S., & Ackerman, A. S. 2018, arXiv:1802.06241
- Guillot, T. 2010, *A&A*, **520**, A27
- Guillot, T., Ida, S., & Ormel, C. W. 2014, *A&A*, **572**, A72
- Hansen, J. E. 1971, *JatS*, **28**, 1400
- Helling, C., Woitke, P., & Thi, W.-F. 2008, *A&A*, **485**, 547
- Hiranaka, K., Cruz, K. L., Douglas, S. T., Marley, M. S., & Baldassare, V. F. 2016, *ApJ*, **830**, 96
- Jacobson, M. Z. 2005, in *Fundamentals of Atmospheric Modeling*, ed. M. Z. Jacobson (Cambridge: Cambridge Univ. Press), 828
- Kataoka, A., Okuzumi, S., Tanaka, H., & Nomura, H. 2014, *A&A*, **568**, A42
- Kataoka, A., Tanaka, H., Okuzumi, S., & Wada, K. 2013, *A&A*, **557**, L4
- Kawashima, Y., & Ikoma, M. 2018, *ApJ*, **853**, 7
- Knutson, H. A., Benneke, B., Deming, D., & Homeier, D. 2014a, *Natur*, **505**, 66
- Knutson, H. A., Dragomir, D., Kreidberg, L., et al. 2014b, *ApJ*, **794**, 155
- Kreidberg, L., Bean, J. L., Désert, J.-M., et al. 2014, *Natur*, **505**, 69
- Krijt, S., Ormel, C. W., Dominik, C., & Tielens, A. G. G. M. 2016, *A&A*, **586**, A20
- Lewis, N. K., Showman, A. P., Fortney, J. J., et al. 2010, *ApJ*, **720**, 344
- Lodders, K. 2003, *ApJ*, **591**, 1220
- Lovas, F. J., & Tiemann, E. 1974, *JPCRD*, **3**, 609
- Madhusudhan, N., & Seager, S. 2011, *ApJ*, **729**, 41
- Magono, C., & Nakamura, T. 1965, *Journal of the Meteorological Society of Japan. Ser. II*, **43**, 139
- Manabe, S., & Strickler, R. F. 1964, *JatS*, **21**, 361
- Marley, M. S., Ackerman, A. S., Cuzzi, J. N., & Kitzmann, D. 2013, in *Comparative Climatology of Terrestrial Planets* (Tucson, AZ: Univ. Arizona Press), 367
- Marley, M. S., & Robinson, T. D. 2015, *ARA&A*, **53**, 279
- Miguel, Y., Kaltenegger, L., Linsky, J. L., & Rugheimer, S. 2015, *MNRAS*, **446**, 345
- Miller-Ricci, E., & Fortney, J. J. 2010, *ApJL*, **716**, L74
- Miller-Ricci Kempton, E., Zahnle, K., & Fortney, J. J. 2012, *ApJ*, **745**, 3
- Morley, C. V., Fortney, J. J., Kempton, E. M.-R., et al. 2013, *ApJ*, **775**, 3
- Morley, C. V., Fortney, J. J., Marley, M. S., et al. 2012, *ApJ*, **756**, 172
- Morley, C. V., Fortney, J. J., Marley, M. S., et al. 2015, *ApJ*, **815**, 110
- Morley, C. V., Knutson, H., Line, M., et al. 2017, *AJ*, **153**, 86
- Narita, N., Fukui, A., Ikoma, M., et al. 2013, *ApJ*, **773**, 144
- Ohno, K., & Okuzumi, S. 2017, *ApJ*, **835**, 261
- Okuzumi, S., Tanaka, H., Kobayashi, H., & Wada, K. 2012, *ApJ*, **752**, 106
- Ormel, C. W. 2014, *ApJL*, **789**, L18
- Parmentier, V., Showman, A. P., & Lian, Y. 2013, *A&A*, **558**, A91
- Pruppacher, H. R., & Klett, J. D. 1997, *Microphysics of Clouds and Precipitation* (Dordrecht: Kluwer)
- Querry, M. R. 1987, *Optical Constraints of Minerals and Other Materials From Millimeter to the Ultraviolet* (Aberdeen Proving Ground, MD: U.S. Army Armament Munitions Chemical Command)
- Robinson, T. D. 2017, *ApJ*, **836**, 236
- Rogers, L. A., & Seager, S. 2010, *ApJ*, **716**, 1208
- Rogers, R., & Yau, M. 1989, *A Short Course in Cloud Physics* (3rd ed.; Oxford: Butterworth-Heinemann)
- Rossow, W. B. 1978, *Icar*, **36**, 1
- Sato, T., Okuzumi, S., & Ida, S. 2016, *A&A*, **589**, A15
- Seager, S., & Sasselov, D. D. 2000, *ApJ*, **537**, 916
- Seinfeld, J. H., & Pandis, S. N. 2006, *Atmospheric Chemistry and Physics: From Air Pollution to Climate Change* (2nd ed.; New Jersey: Wiley)
- Shen, Y., Draine, B. T., & Johnson, E. T. 2008, *ApJ*, **689**, 260
- Shen, Y., Draine, B. T., & Johnson, E. T. 2009, *ApJ*, **696**, 2126
- Southworth, J., Mancini, L., Madhusudhan, N., et al. 2017, *AJ*, **153**, 191
- Stevenson, K. B., Bean, J. L., Seifahrt, A., et al. 2016, *ApJ*, **817**, 141
- Stevenson, K. B., Harrington, J., Nymeyer, S., et al. 2010, *Natur*, **464**, 1161
- Tazaki, R., & Tanaka, H. 2018, arXiv:1803.03775
- Tazaki, R., Tanaka, H., Okuzumi, S., Kataoka, A., & Nomura, H. 2016, *ApJ*, **823**, 70
- Tsiaras, A., Rocchetto, M., Waldmann, I. P., et al. 2016, *ApJ*, **820**, 99
- Valencia, D., Guillot, T., Parmentier, V., & Freedman, R. S. 2013, *ApJ*, **775**, 10
- Venturini, J., Alibert, Y., & Benz, W. 2016, *A&A*, **596**, A90
- Voshchinnikov, N. V., Videen, G., & Henning, T. 2007, *ApOpt*, **46**, 4065
- Wakeford, H. R., Sing, D. K., Kataria, T., et al. 2017, *Sci*, **356**, 628
- Woitke, P., & Helling, C. 2003, *A&A*, **399**, 297
- Ziegler, C. L. 1985, *JatS*, **42**, 1487